Three-Dimensional Entanglement: Knots, Knits and Nets

Myfanwy Ella Evans

January 2011

A thesis submitted for the degree of Doctor of Philosophy
of The Australian National University

Department of Applied Mathematics
Australian National University

Chapter 1

Introduction

Three-dimensional entanglement, including knots, periodic arrays of woven filaments (knits or weavings) and periodic arrays of interpenetrating networks (nets), forms an integral part of the analysis of structure within the natural science. This thesis constructs novel, 3-periodic knits and nets, then tightens them to an 'ideal' shape in order to give geometric inspiration to the many disciplines of science influenced by structure.

A 3-periodic net in three-dimensional Euclidean space ($\mathbb{E}^3$) is a simple[1] 3-connected[2] graph, which is invariant under three independent translations of $\mathbb{E}^3$ [Klee 04]. A 3-periodic weaving in $\mathbb{E}^3$ is an arrangement of infinite one-dimensional space curves, also invariant under three independent translations of $\mathbb{E}^3$. Fig. 1.1 shows a portion of both a net and a weaving: the infinite structure extends infinitely in three directions.

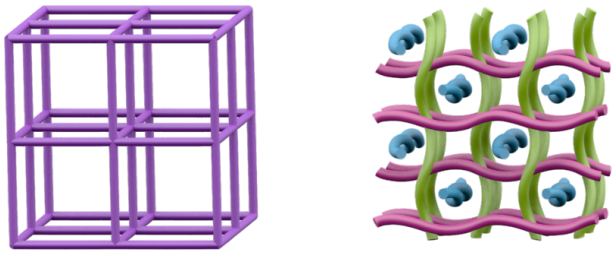

(a) **(b)**

Figure 1.1: A 3-periodic net and a 3-periodic weaving. The net (a) consists of vertices joined by edges and the weaving (b) of filaments that are infinite in length.

The scaffold we use for the construction of 3-periodic knits and nets are Triply-Periodic Minimal Surfaces (TPMS). A minimal surface is a surface with mean curvature of zero: it is equally concave and convex at every point. Every point on the surface is a saddle point,

[1] A simple graph is a set of vertices and edges, where each edge connects a distinct pair of vertices.

[2] A 3-connected graph can have no fewer than 3 vertices (and attendant edges) removed before it forms two or more disconnected components [Gros 92]

except at isolated flat points of zero gaussian curvature, hence the surface is hyperbolic. The term 'minimal' refers to the fact that many of these surfaces minimise the surface area given a set of conditions (boundary constraints, volume constraints, *et cetera*). A soap film on a wire loop is a minimal surface given the constraints of the wire [Dier 92]. TPMS are minimal surfaces that are periodic in three directions: they are invariant under three independent translation vectors.

The genus of an orientable surface (one which has two distinct sides) is a topological invariant defined as the largest number of non-intersecting simple closed curves that can decorate the surface without separating the surface into two distinct components [Stil 87]. Equivalently, the genus of an orientable surface is the number of torus-like handles it forms: the surface of a sphere has genus 0, the surface of a torus has genus 1. The genus of a TPMS is defined by taking a translational unit cell (of the oriented surface) and identifying opposite faces by gluing it modulo translations to obtain a compact surface [Hyde 10]. There are most likely only five highest symmetry TPMS for which this compact surface is genus 3 (a donut with three holes)[3]. These are Schwarz' *Primitive* surface (*P* surface), Schwarz' *Diamond* surface (*D* surface), Schoen's *Gyroid* Surface (*G* surface), Schwarz' *Hexagonal* Surface (*H* surface) and Schwarz' *Cross Layer Parallel* Surface (*CLP* surface) [Fogd 92]. In this thesis, we utilise each of the *P* surface, *D* surface, *G* surface and *H* surface.

To define the *cover* of a surface, we consider a cylinder of infinite length. Any infinite strip of the two-dimensional Euclidean plane ($\mathbb{E}^2$) can be wrapped over the cylinder such that it covers the surface. Thus any infinite strip of $\mathbb{E}^2$ is a *cover* of the infinite cylinder. The *universal cover* of a surface is the cover of all possible covers of that surface, for example the universal cover of the infinite cylinder is $\mathbb{E}^2$. More technically, the *universal cover* of a topological space Y (such as a TPMS), is a *simply connected*[4] space X, along with a *covering map*[5] $f : X \to Y$. The universal cover of a TPMS is the two-dimensional hyperbolic plane ($\mathbb{H}^2$), which can be wrapped over the TPMS, in much the same way as $\mathbb{E}^2$ can be wrapped over a cylinder. To harness the simplicity of a two-dimensional surface as compared with 3D space, tilings of the TPMS are initially constructed as tilings of the

[3]The completeness of these five genus-3 TPMS is still an open question due to the possibility of 'gyroid-like' intermediate surfaces within other families of TPMS.

[4]A domain is *simply connected* if any loop within the domain can be shrunk to a point continuously, *i.e.* the area enclosed by a circle is simply connected, the area between two concentric circles is not [Stil 87].

[5]A *covering map*, from a topological space (X) to another (Y), is a surjective map that is locally a homeomorphism, each point in X has a neighborhood whose image under the covering map in Y is equivalent [Stil 87].

universal cover of the TPMS: $\mathbb{H}^2$. These vertices and edges in $\mathbb{H}^2$ are wrapped over the TPMS, and in turn represent vertices and edges of an array in $\mathbb{E}^3$. For example, Fig. 1.2 shows the vertices and edges of a tiling in $\mathbb{H}^2$, an equivalent tiling wrapped over the *D* minimal surface and the vertices and edges of the tiling that results in $\mathbb{E}^3$.

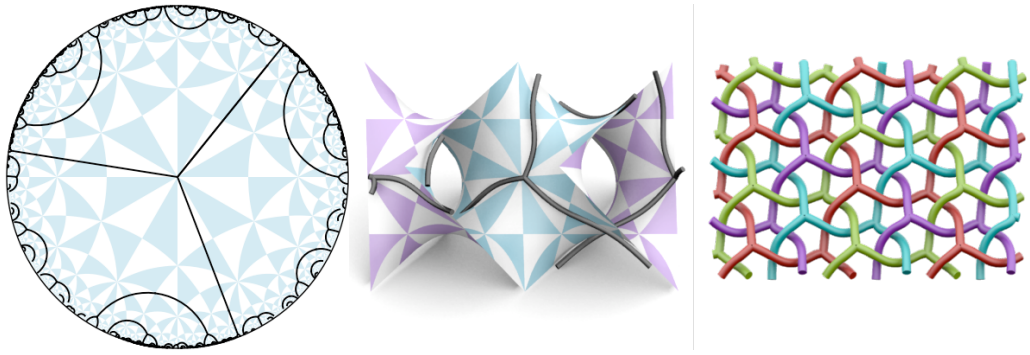

(a) **(b)** **(c)**

Figure 1.2: The vertices and edges of a tiling shown (a) in $\mathbb{H}^2$, (b) wrapped over the *D* minimal surface, and (c) as an entangled structure in $\mathbb{E}^3$.

Furthermore, we numerically tighten the entangled flexible structures to an ideal conformation that minimises the ratio of edge (or filament) length to diameter, which builds on a wide body of work containing the numerical tightening of finite knots and links [Katr 96, Stas 98]. To enable the tightening of periodic entanglements and structures containing vertices, we extend the Shrink-On-No-Overlaps (**SONO**) algorithm [Pier 98], a simple and fast algorithm for tightening finite knots and links.

The ideal geometry of weavings exposes an interesting physical property: *Dilatancy*. The cooperative straightening of the component filaments of a 3-periodic weaving with a fixed diameter induces an expansion of the material in conjunction with an increase in the free volume. We catalogue weavings with varying dilatancy, and predict a dilatant weaving as the alignment of keratin in the corneocytes of the outer 'horny' layer of mammalian skin. The dilatant property of the matrix allows the skin to maintain structural integrity while expanding during the uptake of water.

1.1 Historical Context

Soft condensed matter, including gels, foams, polymers, colloids and liquid crystals display behaviour not necessarily determined by their molecular or atomic structure alone. Interactions of structure assembled at the mesoscale, an intermediate length scale larger

than molecules but smaller than the bulk material, can influence macroscopic behaviour of the material: that which is visible to the naked eye ($> 1mm$). Particularly influential are the geometry and topology of mesoscale structures that self assemble from amphiphilic molecules [Char 85, Hyde 97, Sado 90]. These structures are clearly related to smaller scale patterns found in molecular and atomic crystals.

To understand the structure of chemical frameworks, we may consider their abstraction to geometric objects. A simple approach is the use of homogeneous sphere packings, where atoms are located at sphere centres and bonds at contacts between spheres. Enumeration of periodic structures by homogeneous sphere packings, which catalogues periodic nets of edge length 1, is still incomplete, but leads to a relatively manageable set of physically relevant frameworks [Koch 99, OKee 08]. An extension to this approach is to pack infinite cylinders, where cylinders represent rods of strongly bonded atoms within a chemical framework [OKee 01, OKee 05]. These so-called rod packings have structural stability yet low packing fractions, and are widely identified throughout structural chemistry [OKee 96]. An example of such a rod packing, the cubic Γ rod packing, is shown in Fig. 1.3.

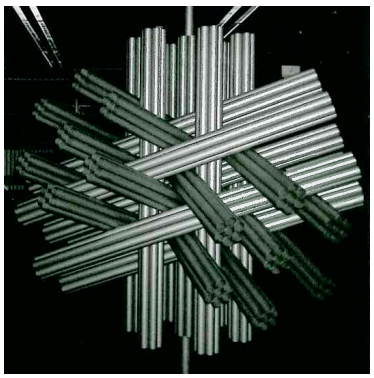

Figure 1.3: Sculpture of the Γ rod packing, located at the Max-Plank-Institut Für Metallforschung, Stuttgart. Photo courtesy of Vanessa Robins.

As another approach, a periodic structure may be considered as a packing of convex, closed, finite cells (polyhedra), where the vertices and edges of the cells within the packing define the net. A simple description of nets constructed in such a way comes from the component polyhedra: this description is known as a *polyhedral* description [OKee 96]. This may also be generalised to polyhedra with curved faces, as well as infinite polyhedra. Details of the use of these packings in new materials can be found in [Lord 06].

Despite these extensive collections of structures, there are still structures that may not

be described by these methods, particularly those that contain multiple interpenetrating nets or weavings of infinite filaments. The TPMS reticulation method presented in this thesis intends to fill these unexplored regions of structure that are not covered by current enumerative techniques.

The energetically favourable assembly of atoms (and molecules) in crystalline arrangements involves (intrinsic) curvature [Hyde 84]. Hanging structures from a TPMS scaffold mimics these conditions in crystalline solids such as Zeolites (microporous aluminosilicate minerals commonly referred to as molecular sieves) and Metal-Organic Frameworks (crystalline compounds consisting of metal ions or clusters coordinated to organic molecules to form porous structures). This curved geometry stems from the diffusion and confinement of interstitial charges within a charged lattice, or alternatively from templating molecules. Supporting this hypothesis, the theoretical framework of some (real) Zeolites were found to reticulate TPMS [Hyde 91, Hyde 93]. Fig. 1.4 shows how the graph of Sodalite, an aluminosilicate, can be considered as a reticulation of the *P* minimal surface. We note that this Sodalite graph also arises as a reticulation of the *D* minimal surface. Frameworks derived from TPMS reticulations may consist of multiple interwoven components, as well as large pore spaces [Chen 01].

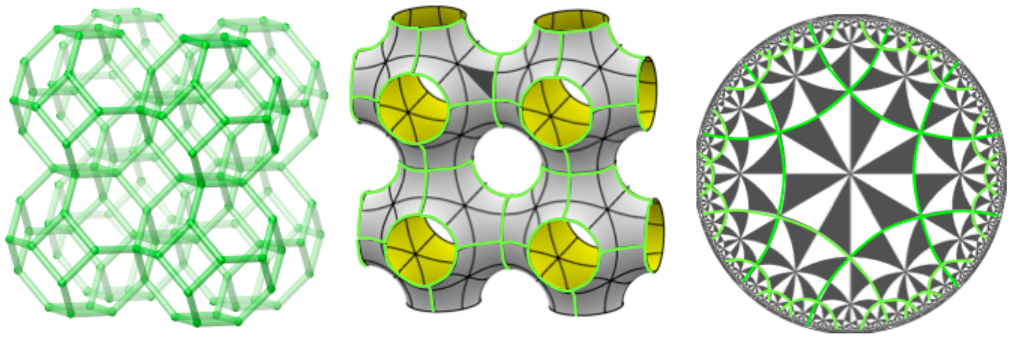

(a) **(b)** **(c)**

Figure 1.4: The Sodalite structure shown (a) in $\mathbb{E}^3$, (b) as a reticulation of the *P* minimal surface, and (c) as a tiling commensurate with the $*246$ tiling in the covering space of the surface, $\mathbb{H}^2$. Image courtesy of [Hyde 10].

If we map decorations in the universal covering space of the TPMS ($\mathbb{H}^2$) to $\mathbb{E}^3$, we allow complex (3D) euclidean geometry to be reduced to simpler (2D) hyperbolic geometry. Tiling the universal cover of a TPMS, discretised by the in-surface symmetries of the surface (rather than $\mathbb{E}^3$ symmetries), dates back to the ideas of Sadoc and Char-

volin [Sado 89]. As candidates for reticulation, decorations of $\mathbb{H}^2$ are restricted based on sub-symmetries and translational symmetries of the TPMS, where the latter restriction guarantees the periodicity of the resulting structures in $\mathbb{E}^3$ [Fogd 92]. Each family of TPMS has a set of in-surface symmetries that dictate allowed symmetry groups in $\mathbb{H}^2$ [Robi 04a, Robi 04b, Robi 05].

The systematic enumeration of commensurate tilings of $\mathbb{H}^2$, those with symmetry that is a subgroup of the maximal 2D symmetry group of the desired TPMS, calls upon the use of Delaney-Dress tiling theory. In the 1980's, Andreas Dress developed a finite symbol to encode both the topology and symmetry of an infinite periodic tiling (on 2D surfaces with positive, zero or negative curvature) using the earlier work of Matthew Delaney: the Delaney-Dress symbol [Dres 87]. The encoding is unique for finite disk-like tiles that fill any simply connected space. Delgado-Friedrichs and Huson harnessed the uniqueness of the Delaney-Dress symbol in developing an algorithmic enumeration of periodic tilings of each of the sphere, plane and hyperbolic plane [Huso 93, Delg 03a].

To obtain an enumeration of such tilings commensurate with the *P*, *D* and *G* surfaces and their corresponding TPMS reticulations is a complex process. The map from $\mathbb{H}^2$ tilings to TPMS tilings is many-to-many due to complications with group automorphisms and the multiply-connected nature of the TPMS. An online enumeration of these tilings (in $\mathbb{H}^2$ and on the TPMS) is located at [Hyde 10], and details of the process given in [Hyde 06]. A complete description of the reticulation of tilings with Kaleidoscopic symmetry is given in [Rams 09]. This work considers tilings of $\mathbb{H}^2$ that are composed entirely of tiles topologically equivalent to a compact disk: this constraint means that all resulting structures in $\mathbb{E}^3$ will be single component, 3-periodic nets. In this thesis, we extend to tilings of $\mathbb{H}^2$ by tiles that are topologically equivalent to infinite ribbons or infinite branched ribbons, *free tilings*, which gives two more classes of structures in $\mathbb{E}^3$: multiple component nets and filament weavings.

Examples of the reticulation of some high symmetry free tilings on TPMS have been published [Hyde 99, Hyde 00a, Hyde 00b, Hyde 00c, Hyde 03a, Hyde 03b, Hyde 03c]. Topology of the vertices and edges remaining in $\mathbb{E}^3$ once the surface is dissolved are examined in these publications, but no approach is detailed as to the analysis of the resulting structure. This thesis will examine a larger set of examples through the extension of the Delaney-Dress tiling theory to include free tilings. This enables easy description of free tilings as well as the scope for an enumeration. We also examine a particular class of these free tilings where the tile boundaries are infinite and vertex-free, which result in TPMS

reticulations that are weavings of curvilinear one-dimensional filaments.

Current techniques for analysis of nets in $\mathbb{E}^3$ that contain either a single component or multiple components include three main approaches: quotient graphs, SyStRe analysis and TOPOS analysis. A few simple methods are also available for the analysis of weavings of one-dimensional filaments: crossing number, minimal crossing number, average crossing number among others. We detail these methods here.

Note that a structure is comprised of three elements: the first is its *topology*, which refers to the abstract graph connectivity of the structure, the second is *ambient isotopy* class, which refers to all structures related to each other by an ambient isotopy[6] and the third is the geometry of the edges of the structure in $\mathbb{E}^3$. We consider each of the current methods in relation to these three elements of structure.

The *quotient graph* of a periodic network is built from a single representative of each translationally equivalent vertex and each translationally equivalent edge. A *labelled quotient graph* labels the edges by their lattice translation vectors in the periodic net [Chun 84]. For example, Fig. 1.5 shows the labelled quotient graph of a periodic graph which follows the edges of stacked cubes (the **pcu** net). Quotient graphs encapsulate the topology of periodic structures. In general however, there is no algorithm for determining when two quotient graphs represent the same periodic net. Further, the labelled quotient graph gives no information about the ambient isotopy class or edge geometry of the structure.

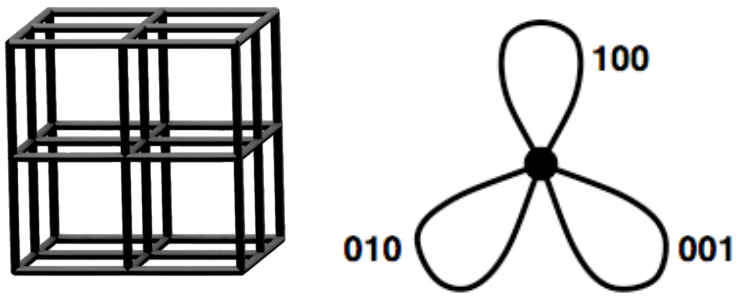

Figure 1.5: (a) The 3-periodic **pcu** net. (b) The labelled quotient graph of **pcu**.

The SyStRe algorithm [Delg] provides an equilibrium (barycentric) placement of vertices (crystalline form) within a labelled crystallographic quotient graph. This placement

[6] An *ambient isotopy* is a continuous deformation of an embedding space. Two nets are equivalent if there is an ambient isotopy from one to the other i.e. one net can be deformed into the other without allowing edges to cross through each other [Crom 04].

gives a system for comparing the topology of periodic nets [Delg 03b]. This canonical form for periodic nets, however, does not prescribe the equivalence of nets within an ambient isotopy class. Furthermore, the SyStRe algorithm is unable to find an equilibrium placement for nets where distinct vertices occupy the same location in an equilibrium placement (vertex collisions) and where distinct edges intersect in the equilibrium placement (edge collisions), and is also unable to relax non-crystallographic nets. Additionally, the algorithm is only able to find a canonical form for single-component nets.

TOPOS analysis of a net [Blat 06] collates the knots formed by single cycles, and links found by disjoint pairs of cycles, in the net. This approach is unique in that fact that it is sensitive to the equivalence of nets by ambient isotopy. An algorithm such as this, based on analysis of interpenetration of rings, is excellent at identifying when two nets belong to distinct ambient isotopy classes, but fails to prove two nets belong to equivalent ambient isotopy classes when their linking signature is equivalent. A further challenge to analysis methods such as this are entanglements that occur on a scale beyond cycles, such as the ravel [Cast 08]. These entanglements have no knotted or linked cycles, yet are still entangled, and hence will be overlooked by the TOPOS analysis. Such an entanglement has been recently synthesised: a finite molecule that forms a ravel is described in [Li 11].

To encompass more general spatial patterns, in particular those of one-dimensional (1D) filaments, we delve into an area examined by polymer physicists and mathematicians alike. The *Crossing Number* of a material is a simple intuitive measure counting the number of times a filament crosses over itself or another. This measure is also used in knot theory to analyse knots and links. A related quantity is the *Minimal Crossing Number*, where an object is manipulated (within an ambient isotopy class) so as to have the minimal number of crossing over itself or other objects [Buck].

To obtain a quantity that is independent of the viewing direction, one may consider an average of the crossing number across all 2D projections of the material (as the crossing number may vary with the chosen perspective). This value is known as the *Average Crossing Number* (ACN). Analysis of materials by the ACN is a geometric problem, involving a specific embedding of a topological object. A quantity associated with the ACN for entangled infinite filaments is how this ACN changes with the increase of the material sample size [Buck]. Another concept related to the ACN is the *temperature* of a tangle [Buck 08]. This considers what portion of a filamentous array is visible from a particular view point: those arrays that are more tangled will have a larger portion of filaments obscured, and thus a higher temperature.

We may also consider the shape of individual filaments within an array: restrictions on the curvature of a filament influences how filaments can tangle together [Buck 07]. This entanglement measure requires some physical thickness to the filament, and a minimisation of an energy associated with the curvature of the filament [Buck 98, Simo 09].

These available methods are far from comprehensive in the analysis of 3-periodic structure, and this is the gap in the literature that we will partially fill with the work in this thesis. To do this, we extend a technique that has been insightful when analysing finite knots and links. The idea is intuitive: take a knot, give it thickness and pull it tight, forming an *Ideal Knot*. To quantify the entanglement of an ideal knot, one must first choose a physical quantity associated with this conformation. There are many energy measures to consider[7], which include the *minimum distance* energy [Simo 94], the *symmetric* energy [Buck 93], [Buck 95], and the *conformal* energy [OHa 91, Dioa 98]. A simple quantity of the ideal conformation is the ratio of length to radius. This quantifies the entanglement of a knot, which is useful in identifying distinct conformation which belong to the same equivalence class by ambient isotopy. Much intuition has been gained in knot theory by considering this energy function of ideal knots [Stas 98].

Figure 1.6: The ideal conformation of a trefoil knot.

A different conformation energy is a compactness energy. The minimisation of this energy in turn minimises the occupied space of the filaments, which represents the structure in a most compact form. This has been considered elsewhere for a single untangled filament, where the result is a helical form [Przy 01]. Interestingly, the pitch given by the compact helix is the same as that of a collagen helix [Mari 00].

For each of these energy quantities, it is difficult to identify the conformation of a knot

[7] A comprehensive summary of energy measures for finite entanglements pre-1998 can be found in [Scha 98]

or link which minimises the energy. A fruitful approach is to computationally tighten any given configuration of the entanglement to a minimal energy state. One such algorithm is simulated annealing [Kirk 84, Laur 98]. Initially, the knot is discretised to a series of vertices and edges, and an energy functional is defined. A random move is applied to any node of the knot trajectory, the energy recalculated and the move either accepted if the energy is less or rejected if the energy is greater. Through the continued application of this process, a local energy minimum is achieved. A similar recipe is given in [Simo 94], which uses random perturbations to decrease the minimum distance energy. Further to this, another process of simulated annealing with some additional measures in place to remove trapping of the structure in local minima is given in [Grze 97]. Finally, an algorithm to relax the energy of a knot is given in [Kusn 97, Dioa 98]. There is no proof, however, that any of these simulated annealing algorithms find a global minimum.

The **SONO** algorithm (*Shrink-On-No-Overlaps* [Pier 98]) is one approach to the computational tightening of knots and links, which minimises the ratio of length to radius as the energy function. It uses a repulsion mechanism to push nearby segments of the knot away, coupled with a shrinking mechanism to tighten the knot. This algorithm is simple and efficient. Mechanisms are in place within the algorithm to shake the knot out of local minimum energy conformations (that are not global energy minima), but a proof that these mechanisms will always ensure the global minimum is reached is still elusive and likely untrue. In this thesis, we will extend the **SONO** algorithm to tighten both 3-periodic knits and nets to optimal forms by minimising the ratio of length to diameter.

We predict that the ideal forms of many of these branched and 3-periodic structures will realise all possible symmetries of the structures, however we see that previous results of the **SONO** algorithm may indicate otherwise. The **SONO** algorithm shows a symmetry breaking effect when tightening torus knots with a high crossing number, and also for the tightening of a periodic double helix [Pier 98], where the ideal form sees one strand of the helix pull straight and the other wind around the outside. We also note that an optimal conformation for the double helix while preventing a symmetry breaking event has also been studied [Olse 10].

1.2 Significant Results

A key body of work to come from this thesis is the construction of an array of structures with a specific embedding, rather than simply a prescribed topology, which are relevant to

the natural sciences. The nets that we construct in this thesis are, in most cases, multiple component interpenetrating nets. Such nets arise frequently in synthetic chemical frameworks, as seen in Ch. 3, and we generate more complex examples of such nets as possible targets for synthesis. In the construction process presented in this thesis, all three elements of the structure are prescribed, including topology, ambient isotopy class and edge geometry, which is in contrast to previous enumeration techniques. We obtain two such edge geometries for a net, one is the geometry of the tile edges as they sit on the TPMS, and the other is the ideal geometry found through simulation. These specific geometries, that are often distinct from SyStRe barycentric embeddings, may yield important material properties.

The 3-periodic entanglements of infinite filaments constructed in this thesis are, in the simplest cases, well recognised rod packings. Through the TPMS reticulation method, we are able to generalise the notion of a rod packing to contain curvilinear as well as rectilinear components, and build a more complete taxonomy of 3-periodic weavings. A catalogue of entanglements of infinite filaments is certainly missing from the current literature, and these new structures may provide insight into weavings of polymers, proteins and DNA.

An interesting consequence of the idealisation of weavings to optimal configurations is the geometry of the filaments is often helical. In many cases, the geometry prescribed by the idealisation is equivalent to that of the weaving as it sits on the TPMS, which implies relevance for the exact filament geometry obtained from the TPMS. The helical geometry of some weavings in their optimal configuration leads to an exotic physical property: *Dilatancy*. In addition to this, it is possible that these ideal weavings may display other interesting physical regimes, such as auxetic behaviour, which is a likely consequence of dilatancy.

These dilatant weavings are attractive design targets for new synthetic materials, stemming from the potent increases in the free volume of the material on straightening of the filaments, while maintaining structural stability of the material. As a bio-material, this beautiful property of the ideal Σ^+ rod packing gives an explanation for the keratin organisation in the corneocytes of the stratum corneum layer of the skin. The dilatancy of the keratin matrix allows us to explain the remarkable structural rigidity of the skin during the uptake of water and subsequent swelling of the skin. The ramifications of knowledge of the keratin organisation are immense: the barrier properties of the skin are important in many areas of the medical and therapeutic sciences, and surely relate to the structural forms of the skin.

1.3 Overview of the thesis

We begin in Ch. 2, titled "Free Tilings of the Hyperbolic Plane", where we extend the Delaney-Dress encoding of conventional tilings of $\mathbb{H}^2$ to include free tilings of $\mathbb{H}^2$, which are tilings by tiles of infinite size. The chapter includes a brief catalogue of such free tilings, that are regular (1-transitive edges, vertices and tiles) and are composed of infinite ribbon tiles with high symmetry. We embed these selected, high symmetry free tilings into either the $*246$ or $*2226$ chart of $\mathbb{H}^2$, so as to be commensurate for projection to the *P*, *D* and *G* surfaces in the former case, and the *H* surface in the latter. Complications arise in the embedding of free tilings with Stellate symmetry (to be defined later), for which there are an infinite number of embeddings commensurate with the TPMS, and we establish rules to systematically enumerate such embeddings.

Of the free tilings we consider, some have tile boundaries consisting of vertices and edges and others have tile boundaries that are vertex-free infinite geodesics. In Ch. 3, titled "Reticulations of Triply-Periodic Minimal Surfaces", the free tilings containing vertices and edges along the tile boundaries are reticulated over the TPMS to give a catalogue of multiple component interpenetrating nets in $\mathbb{E}^3$. We analyse these resulting structures using the standard SyStRe algorithm and TOPOS program to ascertain information about the structure. Additionally, this chapter contains the reticulation of examples of the other genre of free tilings, composed of infinite geodesic tile boundaries. These free tilings give 3-periodic knits composed of infinite tangled filaments when reticulated over the TPMS. We catalogue these structures, and give details about their geometry and entanglement.

Ch. 4, titled "Ideal geometry of branched and periodic structures", extends the SONO algorithm to computationally tighten 3-periodic structures and is capable of tightening entanglements that contain vertices. We lay the foundations of this algorithm by considering tight finite knots, where the tight configuration is previously established in the literature. Finite knotted graphs are tightened to show the reliability of the algorithm at vertices, and further obtain measurements of the $\frac{L}{D}$ energy for a variety of graph embeddings. Various 3-periodic entanglements of infinite filaments, constructed in Ch. 3, are computationally tightened to reveal the geometry of their tight configurations. Finally, we tighten a few selected single component nets to compare the tight configuration with the SyStRe canonical embedding, and include nets where the SyStRe embedding contains vertex collisions. We then consider the multiple component nets constructed on the TPMS to ascertain their ideal geometry.

The physical property of dilatancy for 3-periodic weavings, where the straightening of filaments leads to an unprecedented increase in the free volume of the material, is described in Ch. 5: "Dilatancy of Woven Filament Arrays" . We show examples of several genres: zero dilatancy, finite dilatancy and infinite dilatancy. We finally explore the dilatant weaving Σ^{+}, which we propose as the scheme for keratin organisation within the corneocytes of the outer layer of mammalian skin. The dilatant property of this matrix allows the swelling of the skin in the presence of water without loss of inter-keratin contacts with the corneocyte, which preserves structural stability.

Chapter 2

Free Tilings of the Hyperbolic Plane

A *tiling* is the faces, edges and vertices of a 2D tessellation of a surface, where tiles only intersect along their boundaries and the tiles cover the whole of the surface. A *reticulation* of a Triply-Periodic Minimal Surface (TPMS) is the edges and vertices (not faces) of a tessellation on the surface: these vertices and edges in three-dimensional Euclidean space ($\mathbb{E}^3$), define a structure. Tilings of the covering space of these intrinsically hyperbolic TPMS, *i.e.* tilings of the two-dimensional Hyperbolic plane ($\mathbb{H}^2$), mimic direct tilings of the TPMS when they adhere to a compatible set of isometries of the chosen surface: in-surface symmetries of the TPMS are represented by symmetries of $\mathbb{H}^2$. Tilings that consist of finite tiles with *Coxeter* symmetry, corresponding to Coxeter discrete groups which contain only mirror symmetries, have been previously explored in detail [Rams 09].

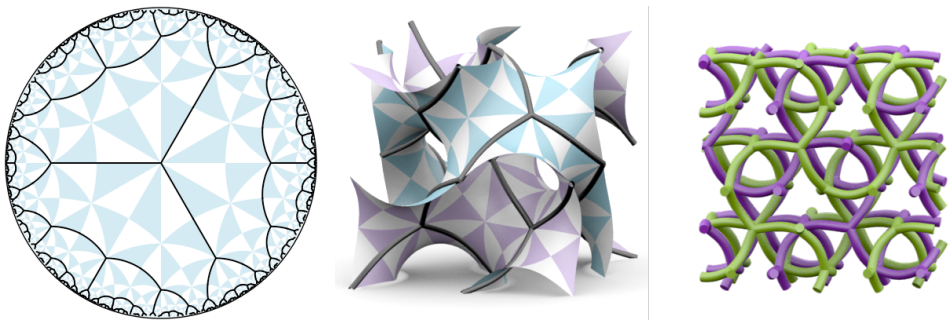

(a) **(b)** **(c)**

Figure 2.1: (a) A free tiling with symmetry $*2223$ in $\mathbb{H}^2$. (b) The tiling shown on one unit cell of the Gyroid surface. (c) The structure remaining in $\mathbb{E}^3$ is two interpenetrating **srs** networks.

This chapter explores tilings of $\mathbb{H}^2$ by tiles of infinite size with an infinite translation as an internal symmetry (*free tilings*). Free tilings are of interest for their form as tilings of TPMS: regular tilings give a single component net in $\mathbb{E}^3$, whereas free tilings give multiple disconnected components in $\mathbb{E}^3$ that are interpenetrating [Hyde 03a, Hyde 00a, Hyde 00c]. For example, Fig. 2.1 shows a free tiling with symmetry $*2223$ in $\mathbb{H}^2$, as a surface tiling of

the Gyroid minimal surface, and as a structure in $\mathbb{E}^3$: two interwoven **srs** nets of equivalent chirality. Further, this chapter extends beyond Coxeter tilings to those with rotational symmetry elements.

This is done by an extension to the Delaney-Dress method for encoding the abstract topology of tilings, which represents the abstract topology of free tilings. In addition, we embed these free tilings firstly into $\mathbb{H}^2$, where an ordering is borrowed from the Euclidean plane, and further into tilings commensurate with the TPMS. To begin, we introduce both orbifolds and the Poincaré Disc model of $\mathbb{H}^2$.

2.0.1 Conceptual Detour: Orbifolds and The Poincaré Disc model

An *orbifold* is the quotient of a manifold by a discrete group of isometries of the manifold [Thur 80]. An orbifold represents a single asymmetric domain of an infinitely repeating pattern along with its symmetry information. More specifically, it is a topological structure where all copies of the repeating pattern are "glued" under appropriate symmetries, such that "unrolling" the orbifold into any covering space results in a repeating pattern. The corner and cone points of this single unit combined with its topology (details of the symmetries of the pattern) gives the orbifold [Conw 92, Conw 02].

A two–dimensional orbifold encodes an infinite pattern on any two–dimensional surface, be it intrinsically Spherical ($\mathbb{S}^2$), Euclidean ($\mathbb{E}^2$) or Hyperbolic ($\mathbb{H}^2$). The isometries of two–dimensional space encoded by such orbifolds are [Conw 92]:

1. Reflections in a line, represented by the orbifold boundary and corner points. A vertex may have n mirror lines incident, denoted by Conway symbol $*\mathtt{n}$. Simply-connected orbifolds containing only reflections are denoted $*\mathtt{ab...c}$ and are called *Coxeter* orbifolds.

2. Rotations, represented by a cone point, denoted by Conway symbol $\mathtt{N}$ denoting a $2\pi/N$ rotation.

3. Translations: the identification of two pair of edges is denoted by $\circ$ (handle), two directions of translational copies symmetry. Topologically, $\circ$ adds a handle to the orbifold, adding to the genus.

4. Glide reflections, involving a reflection and a translation of the motif along the mirror line, denoted by Conway symbol $\times$. Topologically, a $\times$ adds a non–orientable cross–cap structure to the orbifold [Fran 99].

The terminology of orbifolds is combined to form a string of the relevant symmetries of the form AB...C$*$ab...c$\times$...$\circ$.... An arbitrary Conway symbol encodes a realisable orbifold and discrete group, except for the cases $*mn$ and mn where $(m \neq n)$, and also the specific case of $*$m and M, $(m, M > 1)$. These are the only orbifold symbols that do not represent groups [Conw 02].

The combinations of topological features within an orbifold give rise to eight distinct categories, classified by the orientability of simply – or multiply – connected orbifolds, with or without boundaries [Hyde 11]. We describe three of these categories, to be considered later in this chapter. The first is the *Coxeter* orbifolds, which contain only mirror symmetries and correspond to Coxeter groups (Fig. 2.2(a)). This orbifold is a polygonal section of the plane (be it Spherical, Euclidean or Hyperbolic) bounded by mirror boundaries. The second category is the *Hat* orbifolds, which consist of rotational symmetries with a single mirror boundary. The rotational symmetries define the cone points and the mirrors define the boundary (Fig. 2.2(b)). Finally, the *Stellate* orbifolds contain only rotational symmetries, and resemble a pillow punctuated by distinct cone points (Fig. 2.2(c)).

(a) $*$abcd **(b)** A$*$ab **(c)** ABCD

Figure 2.2: (a) A *Coxeter* orbifold: it is bounded by mirror boundaries and corner points. (b) A *Hat* orbifold, it has a single mirror boundary and rotational symmetry. This consists of a cone point bounded by the mirror lines. (c) A *Stellate* orbifold: it has purely rotational symmetry. The orbifold is a pillow punctuated by each of the distinct cone points.

The neat orbifold notation of Conway described above allows us to find directly the *cost* (C) of the orbifold, which is identical to both its Euler–Poincaré characteristic and the area of the orbifold [Conw 92]. The global Gauss–Bonnet formula gives a relationship between the Gaussian curvature of a surface (K) and the Euler–Poincaré Characteristic (χ) [Spiv 79]. More precisely, where A is the given area:

$$2\pi\chi = \iint K \, dA$$

Thus where the Gaussian curvature of the surface is constant, or the area is taken in the universal cover of the surface, the sign of the Euler–Poincaré characteristic gives the sign of the Gaussian curvature of the surface by:

$$K = \frac{2\pi\chi}{A}$$

The cost, C, of the orbifold (and in turn the mean Gaussian curvature) is calculated by:

$$C = 2 - \sum_i d_i$$

The following table shows the value of each d_i.

Symmetry Element	Symbol	d_i
Mirror	$*$	1
Glide Reflection	$\times$	1
n–fold rotation centre	N	$\frac{N-1}{N}$
Mirror Intersection (angle $\frac{\pi}{n}$)	n	$\frac{n-1}{2n}$
Translation (handle)	$\circ$	2

The hyperbolic plane, $\mathbb{H}^2$, has constant negative Gaussian curvature, denying it the luxury of embedding in $\mathbb{E}^3$ without singularities. These singularities manifest as obstructions in the visual representation of $\mathbb{H}^2$in our Euclidean world: immersing $\mathbb{H}^2$ in $\mathbb{E}^3$ with singularities may result in the singularities acting as obstructions to the paths of geodesics [Hilb 52]. This is not ideal for our purposes, and in turn we are led to the Poincaré Disc model of the $\mathbb{H}^2$ [Hilb 52, Coxe 47a, Bear 95].

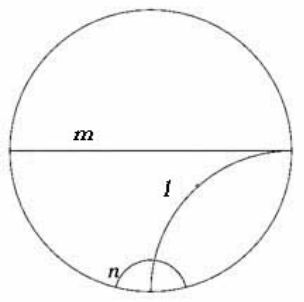

Figure 2.3: The Poincaré Disc: a conformal representation of the $\mathbb{H}^2$. Geodesic paths passing through the centre of the circle, such as m, are represented by straight lines. All other geodesic paths, such as l and n, are represented by circular arcs that intersect the boundary at right angles.

The Poincaré Disc model represents $\mathbb{H}^2$ as the interior of a circle, where $\mathbb{H}^2$ approaches infinity at the boundary of the circle. A geodesic is an arc of the circle that is incident at right angles to the boundary of the circle, as shown in Figure 2.3. Defining the interior of the Poincaré Disc by $\{z \in \mathbb{C} : |z| < 1\}$, the metric for this model is given by

$$ds = \frac{2|dz|}{1-|z|^2}$$

The Poincaré Disc model is a conformal model: Euclidean angles on the disc correspond to angles in $\mathbb{H}^2$. Parallel lines, or "equidistant" lines, in the hyperbolic plane are signified by lines that meet at the disc boundary, *e.g* lines 'l' and 'm' in Fig. 2.3 [Coxe 47a]. "Hyperparallel" lines are represented by non–intersecting lines, *e.g* lines 'm' and 'n' in Fig. 2.3. Fig. 2.4 shows a regular hexagon in both the two–dimensional Euclidean plane ($\mathbb{E}^2$) and $\mathbb{H}^2$, where the Poincaré Disc model is used to represent $\mathbb{H}^2$.

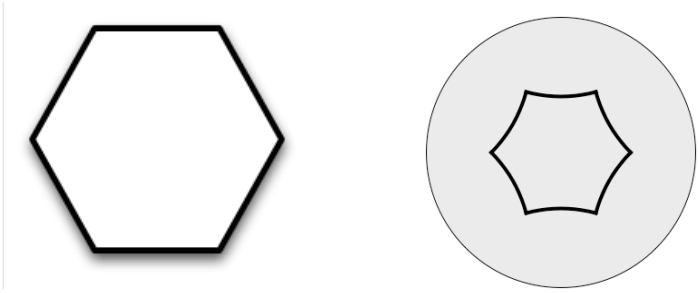

(a) **(b)**

Figure 2.4: (a) A regular hexagon in $\mathbb{E}^2$. (b) A regular hexagon in $\mathbb{H}^2$, shown on the Poincaré Disc model of $\mathbb{H}^2$. It has angles less that 120°.

2.1 Abstract topology of tilings: Delaney–Dress

Conventional tilings

To encode conventional tilings of $\mathbb{H}^2$ (those which are topologically equivalent to a disk), we consider the Schläfli symbol. The Schläfli symbol is of the form $\{p,q,r,...\}$, and encodes regular polytopes and tessellations [Coxe 47b]: a symbol $\{p\}$ encodes a regular ('Platonic') polygon with p sides, a symbol $\{p,q\}$ encodes the tessellation of q regular p–sided polygons around each vertex. Where this tessellation may be embedded in $\mathbb{S}^2$, the symbol defines the polyhedron enclosed by the tiling.

Where the Schläfli symbol encodes only the topology of the tiling, the so–called

Delaney–Dress symbol encodes more information: for any periodic tiling of a two–dimensional plane by tiles of finite size it gives a canonical and finite encoding of the topology and symmetry of the tiling [Dres 87]. Conversely, the Delaney–Dress symbols can be used to build tilings of a given symmetry and topology. The symbol triangulates each tile of the periodic tiling into a series of *chambers*, where the three vertices of the chamber lie at a vertex, edge and face of the tiling respectively. Tilings with the following properties have canonical encodings [Dres 87, Rams 09]:

1. Each tile is topologically equivalent to a disk (they are closed).
2. Tiles only intersect along their boundaries.
3. The size of the tiles is uniformly bounded.
4. Tiles cover the whole of the plane (be it $\mathbb{S}^2$, $\mathbb{E}^2$ or $\mathbb{H}^2$).

Given a tiling of any two–dimensional plane, the construction of the triangulation for the purposes of encoding the topology of the tiling follows a specific recipe:

1. At the barycentre of each tile (the geometric centroid of masses placed at each vertex of the tile), place a vertex denoted '2'.
2. At the midpoint of each edge, place a vertex denoted '1'.
3. At each vertex of the tiling, place a vertex denoted '0'.
4. The domain is triangulated by connecting vertices as shown to the right.
5. 'Colour' the chambers such that those related by isometries of the tiling are the same colour.

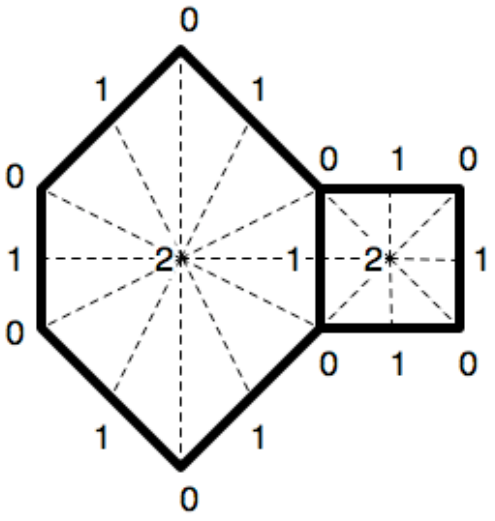

For example, the triangulation of a portion of a tiling of $\mathbb{H}^2$ is constructed using this prescription in Fig. 2.5. A smallest asymmetric unit of the tiling contains two triangular

regions, one shown in red and the other in blue, these two regions represent the two distinct tiles of the tiling. When encoding the tiling, we consider only the chambers within an asymmetric domain: all copies of these chambers are encoded through the adjacency relation information.

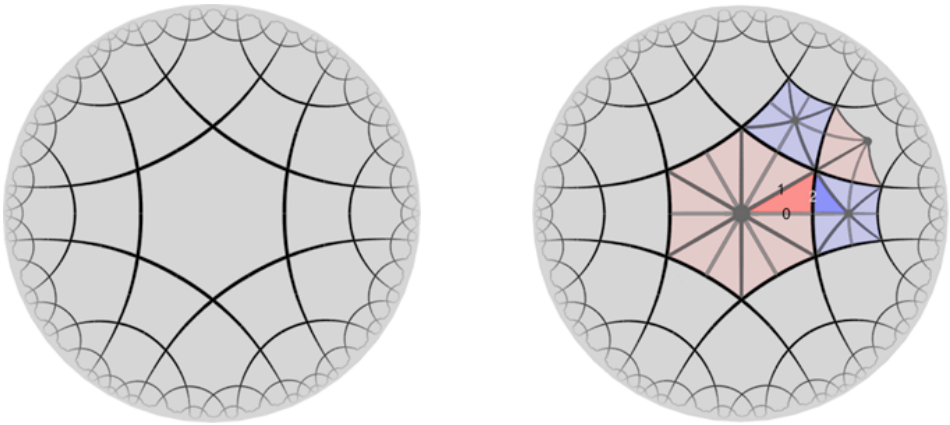

(a) **(b)**

Figure 2.5: (a) A tiling of $\mathbb{H}^2$ by two distinct tiles. (b) A triangulation of an area of the tiling. The triangulation is composed of vertices placed at each of the tile faces, tile vertices and tile edges. This example has two distinct chambers within a asymmetric domain, one shown in red and one shown in blue [Hyde 10].

The 'adjacency map' of each chamber encodes which chambers are adjacent to a selected chamber on each of its boundaries. The term $s0$ denotes the neighbouring chamber across the 0–edge, $s1$ across the 1–edge, and $s2$ across the 2–edge. To encode the topology, we consider the orbits around each of the vertices for each distinct chamber. Around the 2–vertex (the vertex in the centre of the face), we consider how many sets of 0–edges (the edge opposite the 0–vertex) and 1–edges (the edge opposite the 1–vertex) are incident to that 2–vertex. The order of this orbit is denoted $m01$. In general, $m01$ corresponds to the number of edges of a tile. For example, in Fig. 2.5, $m01$ for the red chamber is 6, and $m01$ for the blue chamber is 4. Similarly, we require the order of the 0–vertex orbit, $m12$. For each distinct chambers in Fig. 2.5, $m12$ is of order four. The 1–vertex orbit ($m02$) is always two, by the prescribed construction of triangulation. The full encoding of the tiling shown in Fig. 2.5 is given by the following table:

Chamber Class	$s0$	$s1$	$s2$	$m01$	$m12$
Red	Red	Red	Blue	6	4
Blue	Blue	Blue	Red	4	4

A unique ordering of complexity may be obtained from Delaney–Dress encodings, and in turn these tilings are enumerable up to a given complexity [Delg 03a]. Another approach to encoding the equivalent information is the Generalised Schläfli Symbol [Conw 08]. This is an extension of the Schläfli symbol as it defines a tessellation together with its symmetries, as opposed to an abstract polyhedron. This encoding gives a good visual representation of the tiling. Within this section, however, we use only the Delaney–Dress encoding for tilings of $\mathbb{H}^2$.

Free tilings

To construct and encode tilings of $\mathbb{H}^2$ by tiles of infinite size, termed *free tilings*, we delete edges from a conventional tiling while preserving the original Delaney–Dress triangulation. The term *free tiling* (Vanessa Robins, private communication) is due to the internal symmetry elements of the resulting infinite tile being a free group. These free tilings are denoted by the original Delaney–Dress encoding with an additional signifier, namely a $\bar{1}$–vertex rather than the standard 1–vertex, on the chambers that now contain a 'ghosted' edge. By associating each free tiling with a conventional tiling, free tilings inherit the enumerable structure of Delaney–Dress symbols.

This encoding is complicated by the fact that most free tilings may be constructed from multiple distinct conventional tilings: if two conventional tilings differ only by a single edge (and have different Delaney–Dress encodings), and this particular edge is ghosted, the same free tiling will result and will be classified by two distinct encodings. For example, Fig. 2.6 shows the ghosting of two conventional tilings, where the result is equivalent free tilings.

The unique encoding of a free tiling is chosen to be the simplest among all possible encodings, as defined by the number of chambers within the triangulation of a single orbifold domain. Where there exist multiple simplest encodings of a single free tiling, the unique encoding is chosen to be that which has come from the least complexity Delaney–Dress encoding (Delaney–Dress encodings may be uniquely ordered [Delg 03a]). For example, the encoding of the free tiling shown in Fig. 2.6 part (b) is simpler than that which is shown in part (d).

Two issues arise in finding a unique encoding of a free tiling. Given two distinct encodings, how do we determine if they represent the same free tiling? To find the unique encoding of a free tiling, how do I first enumerate all possible encodings from which to

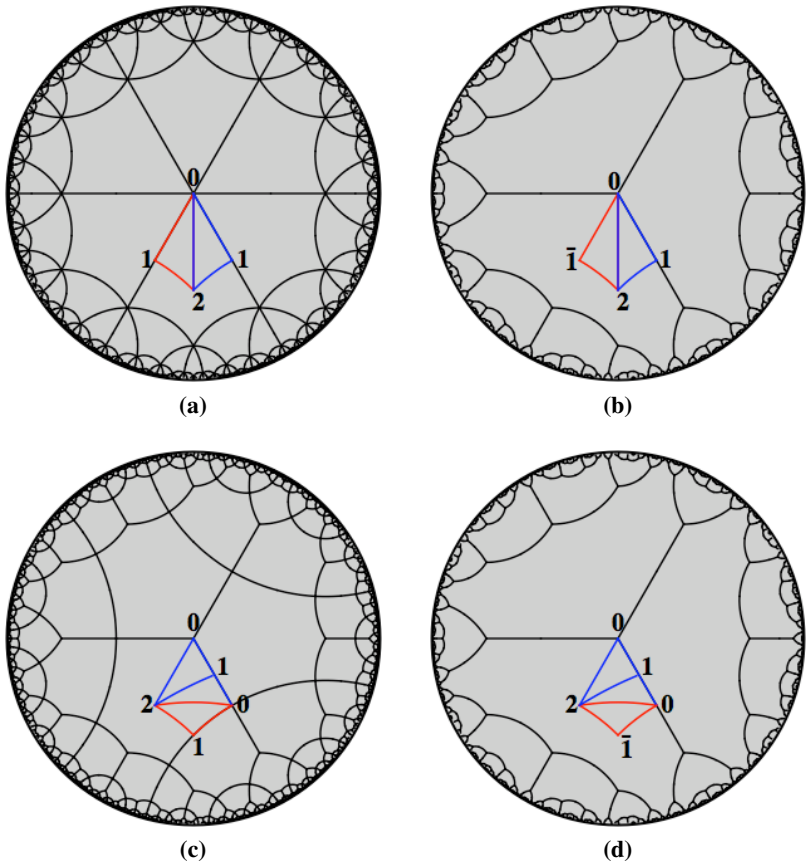

Figure 2.6: (a) A conventional tiling of $\mathbb{H}^2$ shown with its Delaney–Dress encoding. (b) By ghosting a single edge of the conventional tiling shown in part (a), a free tiling of $\mathbb{H}^2$ results, which inherits the Delaney–Dress encoding. (c) A conventional tiling of $\mathbb{H}^2$, which is different from that shown in part (a), shown with its encoding. (d) The ghosting of an edge gives a free tiling which is equivalent to that shown in part (b), yet it inherits a distinct encoding.

choose the simplest? We address these issues through a set of rules that construct the unique encoding of a free tiling from the tile vertices and edges of the free tiling, without information about the conventional tiling from which it originated.

A necessary restriction for the uniqueness of the encoding obtained from this construction process is that we only remove edges from a conventional tiling that leave at least two edges incident at each of its vertices (i.e. the removal of an edge does not remove all edges incident at a vertex), and only remove edges which begin and end at symmetry sites of the orbifold. The completeness of the set of free tilings enumerated with these restrictions is not yet proven, nevertheless this lies outside the scope of this thesis.

We proceed with the construction algorithm. The notation $\bar{1}$ is added to the encoding to represent edges that are present in the conventional tiling but not in the free tiling (ghosted).

We begin with a *parent symbol*, constructed as follows:

1. Identify an asymmetric orbifold domain of the free tiling; this is the domain for triangulation.

2. All symmetry 'corners' of the tile boundary (intersection points of mirror lines or rotation centres) are occupied by 0–vertices. These locations are the only locations where vertices may have been present in the conventional tiling, given the restrictions placed on where edges may be removed from conventional tilings.

3. A 1–vertex is placed at the mid–point of all tile edge segments which connect 0–vertices.

4. All symmetry 'corners' in the interior of the tile with order > 2 are occupied by 2–vertices.

5. All other symmetry 'corners' in the interior of the tile (those with order ≤ 2) are occupied by $\bar{1}$–vertices. This defines all locations where edges may have been removed.

6. A 2–vertex is placed at the mid–point of all orbifold boundary segments in the interior of the tile which connect two $\bar{1}$–vertices.

7. The domain is triangulated where each triangle has a 0–vertex, a 2–vertex and either a 1–vertex or a $\bar{1}$–vertex.

For example, Fig. 2.7 part (a) shows a free tiling of $\mathbb{H}^2$ and part (b) shows the parent symbol of one asymmetric orbifold domain: this triangulation has two 0–vertices at the $*3$ and $*2$ mirror intersections on the tile boundary with a 1–vertex between, and two $\bar{1}$–vertices at each of the $*2$ mirror intersections in the interior of the tile and a 2–vertex between. The triangulation in the example exactly covers a single orbifold domain.

A further process must now take place to find the unique encoding, which is the simplest symbol related to the parent symbol. A simplification may be performed by removing chambers of the encoding (where possible). We then permute through all possible simplifications to find the simplest (and unique) encoding. As simplifications, we wish to remove chambers of the symbol such that we no longer have 0–vertices which are of degree–2 (those which do not lie at actual vertices of the free tiling), and also delete chambers such that we remove as many $\bar{1}$–vertices as possible.

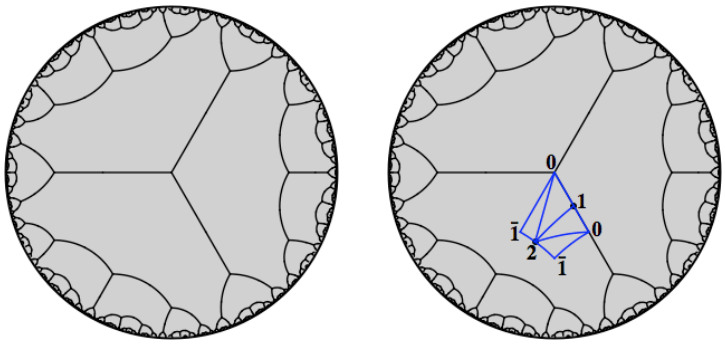

Figure 2.7: (a) A free tiling of $\mathbb{H}^2$. (b) The construction recipe dictates the placement of the vertices and chambers of the parent triangulation, where both $\bar{1}$–vertices are superfluous.

A $\bar{1}$–vertex is a candidate for removal when it is of degree–4 in the full triangulation of $\mathbb{H}^2$ or equivalently of degree-2 in the triangulation of a single orbifold domain, and it is neighboured by a 2–vertex that is not at a symmetry corner. For example, each of the $\bar{1}$–vertices in the parent symbol shown in Fig. 2.7 are candidates for removal. After the removal of a $\bar{1}$–vertex (and its associated edges), the neighbouring 2–vertex slides to the location of the past $\bar{1}$–vertex, and maintains all other connections. This decreases the number of chambers within the symbol by 1, yet the topology and symmetry of the free tiling which it describes is equivalent.

In a similar process, a 0–vertex that lies on an edge of the tiling and is not at a vertex of the tiling is a candidate for removal when it is neighboured by a 1–vertex not at a symmetry corner, and it is also of degree–4 in the full triangulation of $\mathbb{H}^2$ or equivalently of degree–2 in the triangulation of a single orbifold domain. The 0–vertex in the parent symbol shown in Fig. 2.7 is not a candidate for removal as it is of degree–3 in one orbifold domain of the triangulation. After the removal of a 0–vertex (and its associated edges), the neighbouring 1–vertex slides to the location of the past 0–vertex, and maintains all other connections. This process also decreases the number of chambers within the symbol by 1, yet the topology and symmetry of free tiling which it describes is equivalent.

These chamber removals are performed until there are no longer any candidate chambers for removal. It is at this stage that a unique simplest encoding is found. For example, consider the parent symbol shown in Fig. 2.7. Each of the $\bar{1}$–vertices of the encoding are candidates for removal: we note however, that once one is removed, the other is no longer suitable for removal, as its neighbouring 2–vertex will now be on a symmetry corner. We remove each of the $\bar{1}$–vertices, and examine the resulting encodings, as shown in Fig. 2.8.

After the initial chamber removal, the upper encoding in Fig. 2.8 has no further chambers which are suitable for removal. In the lower encoding, however, the 0–vertex of degree–2 is now a candidate for removal. The removal of this chamber, and the subsequent sliding of the 1–vertex gives a simpler encoding of the free tiling. This is the unique encoding of the free tiling.

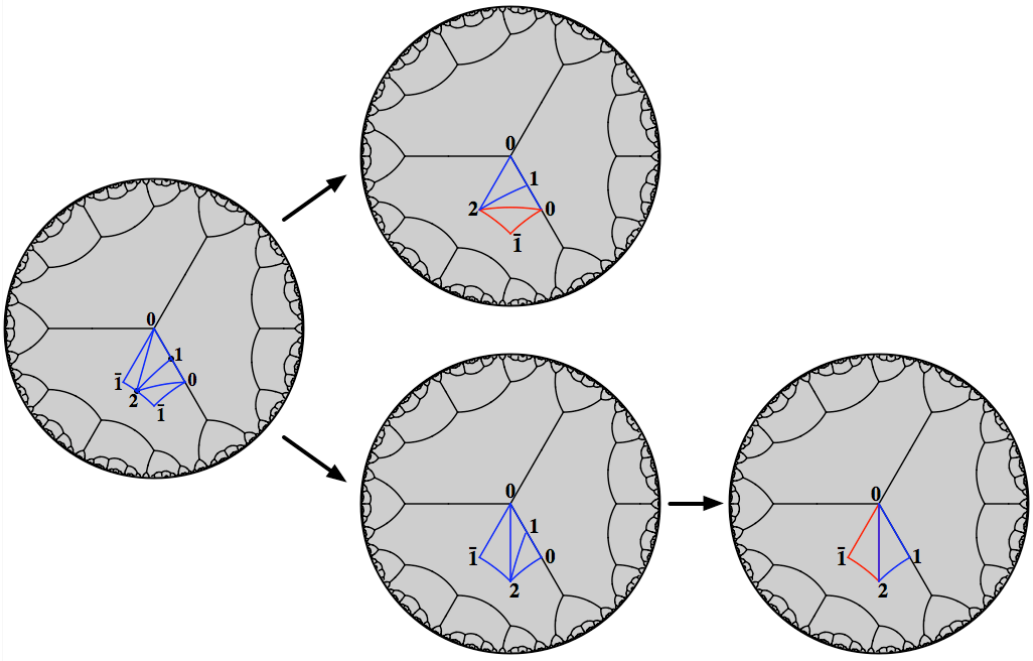

Figure 2.8: The parent symbol of a free tiling in $\mathbb{H}^2$ may be simplified in two ways, which give two distinct encodings. The upper encoding may not be simplified any further, yet the lower encoding may be further simplified by the removal of the 0–vertex of degree 2. This simplification leads to the unique encoding of the free tiling.

We document the encoding from the neighbour maps, as well as the orbits of the 0–vertices and 2–vertices of the chambers. To encode the missing edge, we must note the chamber with the 'ghost' edge. We do this by denoting all chambers with a real (not ghosted) edge in bold and the ghosted edge $\bar{1}$. Denote the chamber shown in blue '*A*' and that shown in red '*B*' to obtain the following tabular representation of the simplest encoding of the free tiling shown in Fig. 2.8:

Chamber Class	s0	s1	s2	m01	m12
A	**A**	B	**A**	4	6
B	B	**A**	B	4	6

2.2 Embedding orbifolds in the universal cover space

The Delaney–Dress symbol is an encoding of the topology and symmetry of a tiling, but not the geometry, for both conventional tilings and free tilings. This encoding is a decoration of an orbifold. An embedding of an orbifold assigns a presentation of the symmetry group encompassed by the orbifold in its universal cover, where a *presentation* is a way to define a group by listing a specific set of elements which generate the group plus a set of relations between the generators. It is trivial to interchange between orbifolds and symmetry groups by choosing a set of generators.

We explore the embedding of orbifolds of the form $*222\mathsf{k}$, $2*2\mathsf{k}$ and $222\mathsf{k}$ in their universal cover. For Coxeter orbifolds, the orbifold is (by definition) bounded by mirrors. When embedded in the covering plane, the positions of the generators (the distinct mirrors) are set uniquely relative to each other as bounding an asymmetric patch. For "hat" orbifolds (with the form $2*2\mathsf{k}$), the relative positions of the generators are uniquely set, which gives a unique embedding into the covering space. The uniqueness of this embedding is obvious if you consider the domain of two orbifolds doubled around the 2–fold rotation: this is a $*2\mathsf{k}2\mathsf{k}$ (Coxeter) domain, which we know uniquely embeds.

Stellate orbifolds have infinite freedom in the relative positions of the generators (rotations) in the covering plane (i.e. infinite scope in the presentation of the group). We wish to systematically generate all distinct presentations of the $222k$ group, so as to specify all distinct embeddings of the orbifold into the covering plane. We begin with the 2222 orbifold, which embeds in $\mathbb{E}^2$ by the orbifold cost formula: $C = 2 - \sum_i d_i = 2 - \left(\frac{1}{2} + \frac{1}{2} + \frac{1}{2} + \frac{1}{2}\right) = 0$.

Embedding the 2222 orbifold into $\mathbb{E}^2$ requires nominating four generating 2–fold rotation sites. Fig. 2.9(a) shows an embedding, where the generators are at the positions $\{0,0\}$, $\{1,0\}$, $\{1,1\}$ and $\{0,1\}$ of $\mathbb{E}^2$. This results in the set of all elements (not just the generators) of the infinite group being grid points in $\mathbb{Z} \times \mathbb{Z}$ (the two–dimensional integer grid: elements are represented by a couple $\{x,y\}$ where x and y are integers).

Given the reference frame established by the embedding in Fig. 2.9(a), distinct presentations of the same group may be obtained by expressing the generators as other elements of the group (i.e. other points in the plane) [Coxe 72]. Labelling the 2–fold rotations located at $\{0,0\}$, $\{1,0\}$, $\{1,1\}$ and $\{0,1\}$ as Q_T, Q_A, Q_B and Q_C respectively, presentation of the group given by the reference frame is

$$< \{Q_T, Q_A, Q_B, Q_C\} : (Q_A)^2 = (Q_B)^2 = (Q_C)^2 = (Q_T)^2 = I, Q_T = Q_A Q_B Q_C >$$

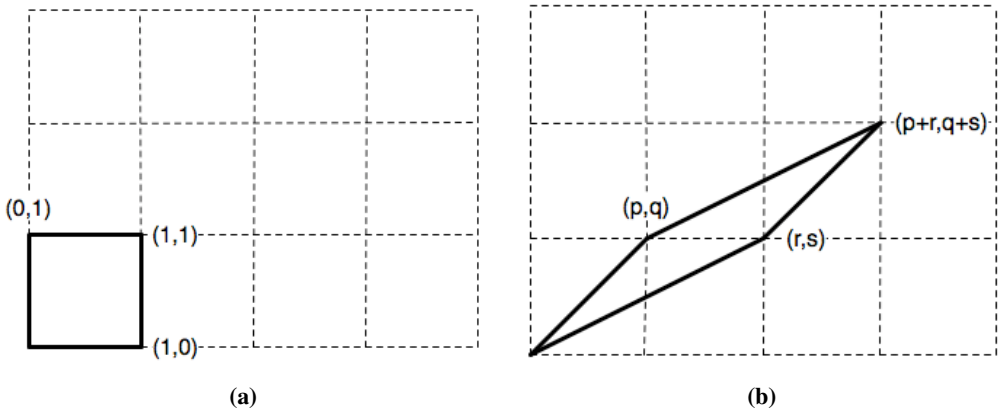

Figure 2.9: (a) An embedding of the 2222 orbifold in $\mathbb{E}^2$. The corners of the square coincide with the points $\{0,0\}$, $\{1,0\}$, $\{1,1\}$ and $\{0,1\}$, establishing a reference frame of $\mathbb{Z}\times\mathbb{Z}$ for subsequent embeddings (b) Another embedding of 2222 relative to the established reference frame.

A new presentation of the same symmetry group specifies generators Q'_T, Q'_A, Q'_B and Q'_C with respect to the reference frame such that the group relations are preserved. Thus we express the generators in terms of the original Q_T, Q_A, Q_B and Q_C.

The set of possible presentations may be represented through parallelograms on $\mathbb{Z}\times\mathbb{Z}$. To reduce duplication of embeddings, we begin by considering only one quadrant of $\mathbb{E}^2$ and we pin the 2–fold rotation Q_T in place, so as to eliminate the possibility of constructing a domain of equivalent shape translated by some vector. We require that the only isometries of the parallelograms are the 2–fold rotations at the corners and that the enclosed area must be 1 (area equivalent to the square in the reference frame embedding), as all cuttings of the orbifold must span the same area. These restrictions are equivalent to satisfying the group relations for a presentation. Note also that this domain is the area enclosed by the four distinct 2–fold rotations, and that a full 2222 symmetry group is double this quadrilateral over any of its edges, where this full domain has area exactly 2 units.

As an example, Fig. 2.9(b) shows a unit area parallelogram on $\mathbb{Z}\times\mathbb{Z}$ with corners $\{0,0\}$, $\{r,s\}$, $\{p+r,q+s\}$ and $\{p,q\}$. Each grid point in the plane represents elements of the infinite group, hence we may express the corner points of the parallelogram (with respect to the reference frame) as:

$$Q'_A = Q_B Q_C Q_B \qquad Q'_C = Q_B$$
$$Q'_B = Q_B Q_C Q_B Q_A Q_B Q_C Q_B \qquad Q'_T = Q_T$$

It is simple to show that the group relations $(Q'_A)^2 = (Q'_B)^2 = (Q'_C)^2 = (Q'_T)^2 = I$ are

satisfied for these new generators. The other group relation, where $Q'_A Q'_B Q'_C$ must be equal to Q'_T, is also satisfied by these elements (working shown below), hence the generators Q'_T, Q'_A, Q'_B and Q'_C are a presentation of the symmetry group of the 2222 orbifold.

$$\begin{aligned}
Q'_A Q'_B Q'_C &= Q_B Q_C (Q_B Q_B) Q_C Q_B Q_A Q_B Q_C (Q_B Q_B) \\
&= Q_B (Q_C Q_C) Q_B Q_A Q_B Q_C && \textit{using } (Q_B)^2 = I \\
&= (Q_B Q_B) Q_A Q_B Q_C && \textit{using } (Q_C)^2 = I \\
&= Q_A Q_B Q_C && \textit{using } (Q_B)^2 = I \\
&= Q_T \\
&= Q'_T
\end{aligned}$$

Enumeration of all such embeddings of parallelograms of unit area in $\mathbb{Z} \times \mathbb{Z}$ may be thought of as a 3–parameter family: the 5 parameters $\{p,q\}$, $\{r',s'\}$ and k, reduce to 3 when the area of the parallelogram is expressed as $ps' - r'q = 1$. To ensure that no additional symmetry points are located on the boundary of the parallelogram, the $\{p,q\}$ (or Q'_C) corner of the parallelogram is chosen such that $\{p,q\}$ are coprime. One solution of the other corner of the parallelogram, $\{r',s'\}$ (or Q'_A) is chosen such that the parallelogram has unit area. For a given $\{p,q\}$, the full set of solutions for the other corner is $\{r,s\} = \{r',s'\} + k\{p,q\}$. This 3–parameter family describes all embeddings of 2222 into a discretised $\mathbb{E}^2$.

The orbifold 2223 has $\mathbb{H}^2$ as the universal cover, as given by the cost formula:

$$C = 2 - \sum_i d_i = 2 - \left(\frac{1}{2} + \frac{1}{2} + \frac{1}{2} + \frac{2}{3}\right) = -\frac{1}{6}$$

Begin by choosing an embedding of the orbifold to be a reference frame in $\mathbb{H}^2$, nominating four generators to present the symmetry group: Q_T, Q_A, Q_B and Q_C. Consider the quadrilateral formed by connecting the four generating elements of the group (Fig. 2.10(a)), establishing a reference frame and discrete infinite grid.

The group relations for the 2223 symmetry group are given by

$$< \{Q_T, Q_A, Q_B, Q_C\} : (Q_A)^2 = (Q_B)^2 = (Q_C)^2 = (Q_T)^3 = I, Q_T = Q_A Q_B Q_C >$$

Fig. 2.10(b) shows a quadrilateral whose four corner points are elements of the infinite group 2223. To establish if the corner points represent generators of the group, and hence

if the quadrilateral is a valid presentation of the group, we consider the group relations. The corner points of the quadrilateral may be expressed as:

$$\begin{aligned} Q'_T &= Q_T \\ Q'_A &= Q_B Q_C Q_B \\ Q'_B &= Q_B Q_C Q_B Q_A Q_B Q_C Q_B \\ Q'_C &= Q_B \end{aligned}$$

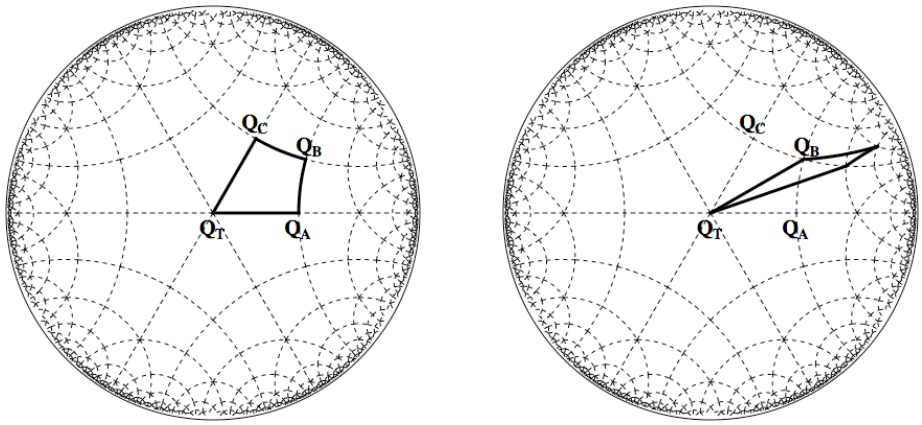

Figure 2.10: (a) An embedding of the 2223 orbifold into $\mathbb{H}^2$. The corners of the quadrilateral are a reference frame grid for other embeddings. (b) A subsequent embedding of the 2223 orbifold into $\mathbb{H}^2$ relative to the reference frame established previously.

It is straightforward to see that the group relations $(Q'_A)^2 = (Q'_B)^2 = (Q'_C)^2 = (Q'_T)^3 = I$ are satisfied for these elements. The other group relation, where $Q'_A Q'_B Q'_C$ must be equal to Q'_T, is also satisfied, with working shown below, and hence the quadrilateral shown is a valid embedding of the 2223 orbifold in $\mathbb{H}^2$ given the reference frame.

$$\begin{aligned} Q'_A Q'_B Q'_C &= Q_B Q_C (Q_B Q_B) Q_C Q_B Q_A Q_B Q_C (Q_B Q_B) \\ &= Q_B (Q_C Q_C) Q_B Q_A Q_B Q_C && \text{using } (Q_B)^2 = I \\ &= (Q_B Q_B) Q_A Q_B Q_C && \text{using } (Q_C)^2 = I \\ &= Q_A Q_B Q_C && \text{using } (Q_B)^2 = I \\ &= Q_T \\ &= Q'_T \end{aligned}$$

To enumerate possible embeddings, we determine possible locations of the Q'_C generator with respect to the reference frame: the analogue of finding the coprime $\{p,q\}$ vertex of the parallelogram. We fix the Q_T generator as an origin, and consider a $\frac{\pi}{3}$ sector of the plane, as all others will be equivalent by symmetry (as was the case for the $\frac{\pi}{2}$ sector of 2222 in $\mathbb{E}^2$). The edge from the origin to Q'_C must not intersect any image of itself.

Consider a 3–fold rotation site, ▲$_0$, in Fig. 2.11(a) to be at the origin, along with an image of the origin by a 2–fold operation, shown as the 3–fold rotation site ▲$_1$. Any geodesic ray from the origin (whose end will be the location of Q'_C) will have exactly three copies radiate from ▲$_1$, one in each of the sectors W_1, W_2 and W_3. If Q'_C (the end of the geodesic ray) is placed in the sector W_3, as shown by the blue geodesic in Fig. 2.11(b), it certainly intersects an image of itself radiating from ▲$_1$. This prohibits the placement of Q'_C in the sector W_3.

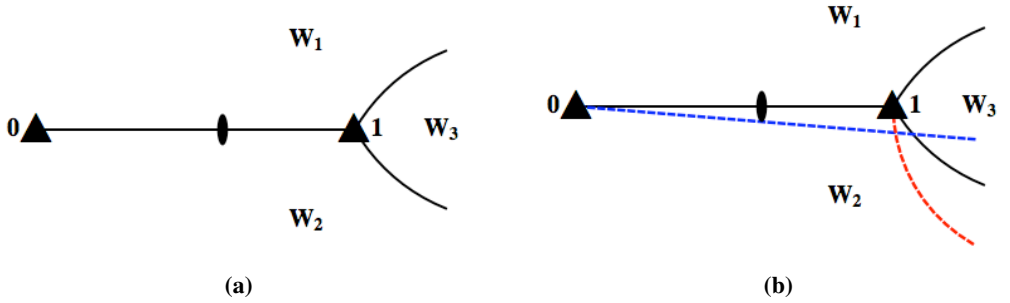

Figure 2.11: (a) The configuration of the 3–fold rotation at the origin (▲$_0$) and an image (▲$_1$), where ▲$_1$ divides $\mathbb{H}^2$into three sectors, W_1, W_2 and W_3. (b) If Q'_C (the end of the blue geodesic) is located in the W_3 sector, the edge from the origin to Q'_C (the blue geodesic) will certainly intersect an image of itself, as shown by the red geodesic.

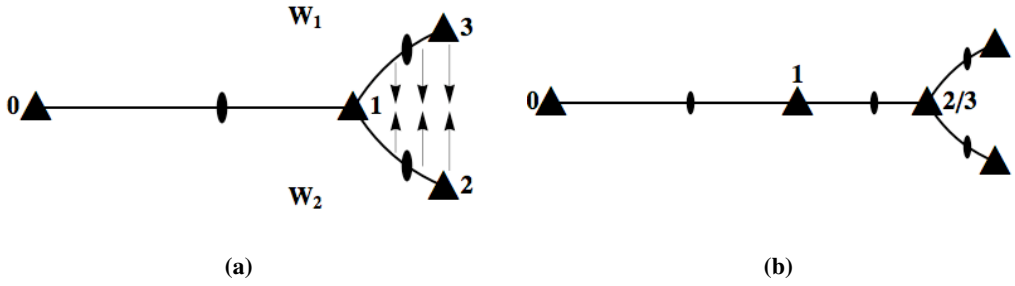

Figure 2.12: (a) The sector W_3 can be excised and the boundary sewn together to form a boundary free plane. (b) The result is a line of 2–fold rotations, terminating at a new 3–fold rotation. Repeating the cutting process further removes territory from where Q'_C is prohibited.

We then remove this prohibited sector (to infinity) from $\mathbb{H}^2$. Fig. 2.12(a) shows how

we may then sew up the remaining boundary to make the space boundary free once again. The result is shown in Fig. 2.12(b), the 3–fold rotation $\blacktriangle_1$ has now become a 2–fold rotation, and the 3–fold rotations $\blacktriangle_2$ and $\blacktriangle_3$ have been joined. By use of the same argument on this new configuration, further W_3 sectors of the plane can excised and the boundary sewn, resulting in an infinite line of 2–fold rotations on a boundary free plane. These prohibited sectors are shown on the 2223 discretisation of $\mathbb{H}^2$ in Fig. 2.13.

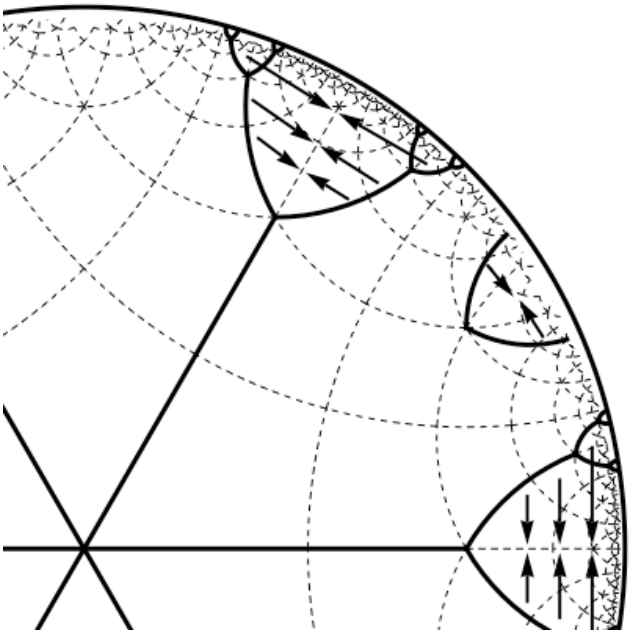

Figure 2.13: Prohibited sectors of the 2223 discretisation of $\mathbb{H}^2$ are shown. There are infinitely many prohibited sectors, located at every 3–fold rotation of the discretisation, where only three such sectors are shown here. The remaining 'allowed" section is a Euclidean subdomain of $\mathbb{H}^2$.

Reducing every 3–fold rotation of the discretisation of $\mathbb{H}^2$ to a 2–fold rotation transforms the discretisation to exactly the 2222 symmetry group, hence, by the orbifold cost formula, we are left with a discretisation of $\mathbb{E}^2$. The removal of sectors of the Hyperbolic plane and subsequent sewing of the boundaries has resulted in exactly a boundary free Euclidean plane.

By only removing territory in which the Q'_C location is prohibited, we have shown that the scope of possible locations of Q'_C are in a Euclidean subset of $\mathbb{H}^2$, discretised by exactly $\mathbb{Z} \times \mathbb{Z}$. The same geometric argument may be used to show that the edge from the origin to Q'_A is also limited to also lie within $\mathbb{E}^2$ discretised by $\mathbb{Z} \times \mathbb{Z}$. The location of Q'_B is then completely determined by Q'_A and Q'_C.

As a result of this ordered Euclidean subdomain of $\mathbb{H}^2$, we may index all possible

quadrilateral domains of the 2223 orbifold exactly by embeddings of parallelograms of unit area in $\mathbb{Z}\times\mathbb{Z}$. Fig. 2.14 shows the $\mathbb{Z}\times\mathbb{Z}$ grid within a $\frac{\pi}{3}$ sector of the discretisation of $\mathbb{H}^2$ by the 2223 reference frame embedding.

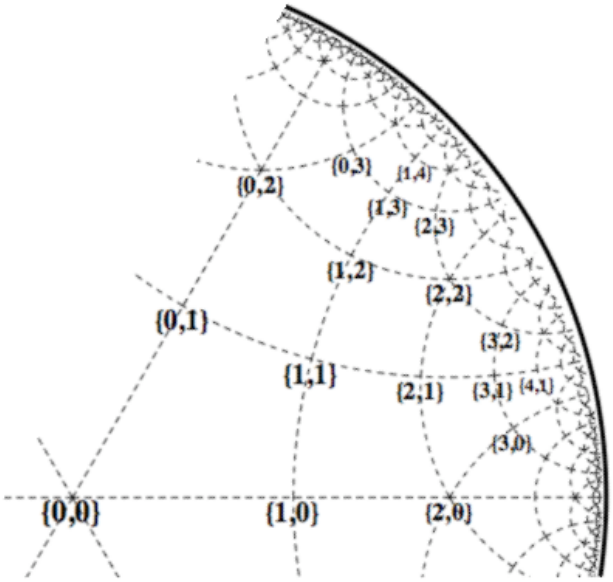

Figure 2.14: The positioning of the grid points of $\mathbb{Z}\times\mathbb{Z}$ in a $\frac{\pi}{3}$ sector of 2223 discretisation of $\mathbb{H}^2$.

An equivalent process may be applied to any 222k discretisation of $\mathbb{H}^2$. The rotational symmetry at each k–fold vertex always restricts the location of the Q'_C generator to be within the adjacent sector, and hence any 222k discretisation of $\mathbb{H}^2$ has an allowed subdomain for the embedding of the orbifold that is equivalent to the 2222 discretisation of $\mathbb{E}^2$ within a $\frac{2\pi}{k}$ sector.

2.3 Embedded tilings commensurate with TPMS

Reticulation patterns of a TPMS must be commensurate with the sub–symmetries of the chosen surface. The 2D asymmetric patch of each of the P, D and G surfaces is a triangle bounded by in–surface mirrors meeting at angles of $\pi/2$, $\pi/4$ and $\pi/6$ at the corners of the patch. The asymmetric patch corresponds to a single $*246$ triangle uniquely embedded in $\mathbb{H}^2$, whose generators are mirrors R_1, R_2 and R_3: the reflection R_1 maps across the line passing from $*6$ though $*2$ vertices, R_2 from $*2$ through $*4$ vertices and R_3 from $*6$ through $*4$ vertices [Robi 04a, Moln 02]. The infinite $*246$ pattern is shown in Fig. 2.15(a). Similarly for the H surface, the smallest asymmetric patch of the surface is a quadrilateral bounded by in–surface mirrors meeting at angles of $\pi/6$, $\pi/2$, $\pi/2$ and $\pi/2$ at each of the

corners [Robi 04b]. This has hyperbolic orbifold $*2226$, and one example of this orbifold is shown in the universal cover of the H surface ($\mathbb{H}^2$) in Fig. 2.15(b).

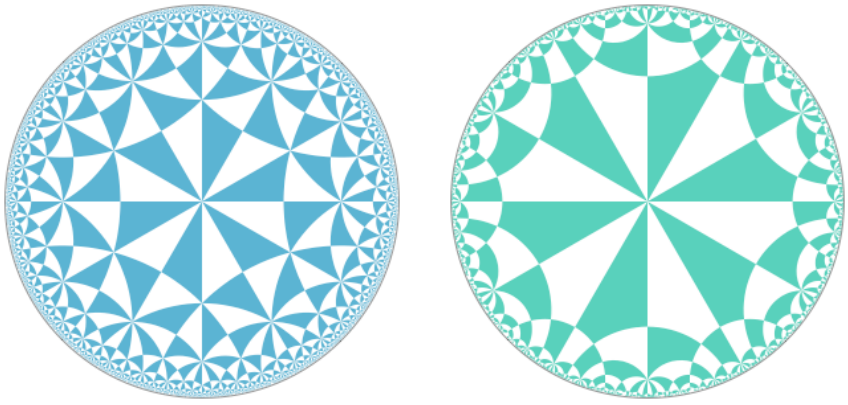

(a) **(b)**

Figure 2.15: $*246$ and $*2226$ tilings represented on the Poincaré Disc model of $\mathbb{H}^2$. The tilings are coloured by an orientation preserving subgroup.

The H surface has a degree of freedom corresponding to a deformation of the surface along the z–axis (variation of the ratio of a to c in the lattice parameters) [Hyde 03b]. This gives a degree of freedom in the asymmetric patch, and a degree of freedom in the $*2226$ tiling of $\mathbb{H}^2$. The $*2226$ tile in $\mathbb{H}^2$ can be divided into two triangles, with the first having angles $\pi/6$, α and β, and the second having angles $\pi/2-\alpha$, $\pi/2-\beta$ and $\pi/2$. The angles α and β are related using hyperbolic trigonometric identities to give:

$$\frac{cos(\alpha)cos(\beta)+cos(\pi/6)}{sin(\alpha)sin(\beta)} = \frac{sin(\alpha)sin(\beta)}{cos(\alpha)cos(\beta)}$$

This results in a one–parameter family of asymmetric domains for $*2226$ [Hyde 03b], given by the following association:

$$cos(\alpha) = \sqrt{1-\frac{13}{16}cos^2(\beta)} - \frac{\sqrt{3}}{4}cos(\beta)$$

Surface reticulations are also chosen adhere to the translational symmetries of the TPMS: "$\circ\circ\circ$" (in Conway's notation), as one primitive unit cell of the oriented (coloured) TPMS has integral curvature -8π, which corresponds to genus–3 with gluings. In doing so, we ensure that reticulations are continuous over the primitive unit cell boundaries, and also display all translations of the TPMS [Rams 09, Robi 04a, Robi 04b].

The combination of these symmetry requirements restricts possible reticulations of

the surfaces to come from particular decorated orbifolds. Specifically, reticulation of the *P*, *D* and *G* surfaces must have decorated orbifolds within the quotient group $*246/\circ\circ\circ$: the orbifold must be a subgroup of $*246$, yet always contain $\circ\circ\circ$ symmetries. The 131 possible orbifolds has been enumerated [Robi 04a], and this list of numbered groups are presented in Appendix A. Likewise, reticulations of the *H* surface must have decorated orbifolds within the quotient group $*2226/\circ\circ\circ$: the orbifold must be a subgroup of $*2226$, yet always contain $\circ\circ\circ$ symmetry. The 32 possible orbifolds commensurate with the *H* surface are also enumerated [Robi 04b], and this numbered list is also presented in Appendix A.

Before embedding with a commensurate symmetry, we must consider our final goal: structures in $\mathbb{E}^3$. Where two reticulations of a single TPMS are related by an intrinsic surface symmetry which lifts to a Euclidean isometry of 3D space, they are called conjugates, and we wish to consider only one representative within a conjugacy class. In hyperbolic terms, this indicates that tilings of $\mathbb{H}^2$ that are related by a symmetry of the underlying surface tiling ($*246$ or $*2226$) are considered within the same conjugacy class. An example of two tilings of $\mathbb{H}^2$ that are related by a symmetry of $*246$, and will give equivalent surface frameworks, is shown in Fig. 2.16.

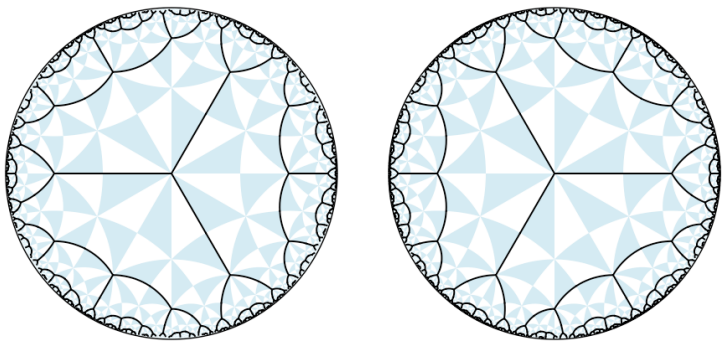

Figure 2.16: Two free tilings with symmetry $*2223$ (group 124 [Robi 04a]) that are related by a reflection of the $*246$ tiling shown behind the tiling. These tilings fall within the same conjugacy class, and they give equivalent frameworks on the TPMS.

The embedding into $*246$ or $*2226$ requires us to express the reference frame generators of the group in terms of the generators of the underlying tiling. For Coxeter and Hat orbifolds, we must take into account automorphic embeddings of the orbifold. An automorphism of an orbifold is an abstract symmetry of the orbifold. Where the automorphism of an embedded orbifold is not a symmetry within the underlying tiling, automorphic em-

beddings of a tiling, which are images of each other through the abstract symmetry, will give distinct surface patterns. An example of two automorphic embeddings of the ∗2224 orbifold, which gives two distinct tilings not related by a symmetry of ∗246, is shown in Fig. 2.17. For Stellates, enumeration of embedded parallelograms into the reference frame accounts for all automorphic embeddings.

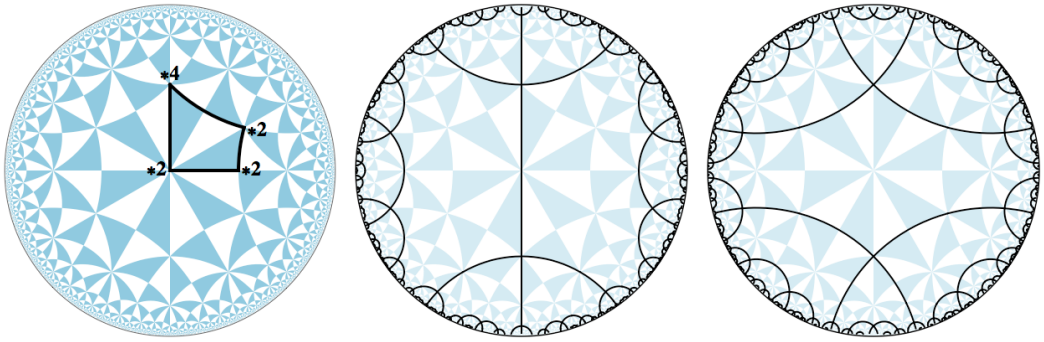

Figure 2.17: (a) Unique embedding of the ∗2224 (group 123 [Robi 04a]) orbifold into the ∗246 tiling, where the abstract symmetry of the orbifold is now asymmetrised. (b,c) Two regular ribbon tilings related by an automorphism of ∗2224.

Regular ribbon tilings and their complements

A *regular ribbon tiling* is a tiling by infinite ribbons that has 1–transitive edges (one type of tile edge), 1–transitive vertices (one type of tile vertex) and 1–transitive tiles (one type of tile face). A *complementary* tiling, related to a regular ribbon tiling, has tile vertices and faces interchanged, and edges interchanged with ghosted edges. Complementary tilings are equivalent to regular, dense forests in alternative nomenclature [Hyde 00a][1]. This terminology is compatible with that for standard tilings.

In a regular ribbon tiling, 1–transitive edges imply that the degree–3 vertex of the tile boundary must have either 3–fold symmetry or ∗3 symmetry. Further, 1–transitive vertices indicate that an edge must have a midpoint at either a 2–fold rotation or ∗2 site. The translation within a tile may be defined by some combination of ∗2 symmetries, 2–fold rotations, '○' or '×'. Of the groups within the ∗246/○○○ quotient group, 4 groups fit these criteria: ∗2223 (group 124), 2∗23 (group 129), 2223 (group 118), and 23× (group 121). We find that simple decorations, such as regular ribbon tilings, on the 23× orbifold

[1] Regularity is an equivalent term in the two schema: *i.e.* in a dense forest, the tile between neighbouring trees is a ribbon.

has increased symmetry of $2*23$ (a supergroup of $23\times$), thus we disregard decorations of this orbifold. We consider regular ribbon tilings and their complements on the three remaining orbifolds, and their embedding into the $*246$ chart of $\mathbb{H}^2$.

The abstract orbifold $*2223$ supports a regular ribbon tiling with a decorative edge passing from the $*3$ location along the mirror boundary to a $*2$ site. The decoration has boundary vertices at the $*3$ corner, edge midpoints at the $*2$ corner, and an infinite translation generated by the parallel mirrors of the remaining two $*2$ corners. This decoration is shown in Fig. 2.18 along with a table representing its Delaney–Dress encoding. We refer to this tiling by the name 124*R*: the **R**egular ribbon tiling of group 124.

Chamber Class	s0	s1	s2	m01	m12
A	**A**	B	**A**	4	6
B	B	**A**	B	4	6

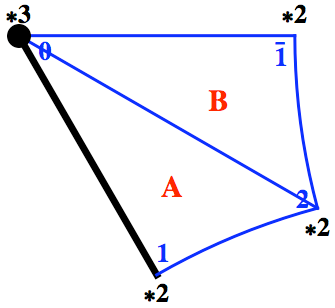

Figure 2.18: The Delaney–Dress representation of a regular ribbon tiling on the $*2223$ orbifold: 124*R*. The edge passes along the mirror boundary from the $*3$ site to the $*2$ site.

The complement of the regular ribbon tiling on $*2223$ interchanges the 0–vertex and 2–vertex sites of the triangulation as well as the 1–vertex and $\bar{1}$–vertex sites. This process swaps the boundaries of the tiles with the infinite translation axes of the tiles. The Delaney–Dress encoding of the complementary regular ribbon tiling of $*2223$ is shown in Fig. 2.19. We call this tiling 124*C*: the **C**omplementary tiling of group 124.

Chamber Class	s0	s1	s2	m01	m12
A	A	**B**	A	6	4
B	**B**	A	**B**	6	4

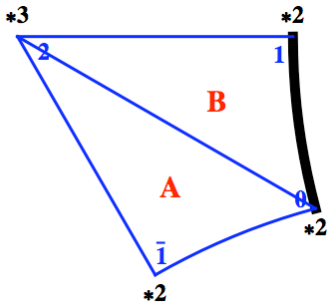

Figure 2.19: The Delaney–Dress coding of the complementary tiling on the $*2223$ orbifold: 124*C*. It is obtained by interchanging the 0–vertex and 2–vertex sites and the 1–vertex and $\bar{1}$–vertex sites of the regular ribbon tiling.

The $*2223$ orbifold has a unique embedding into the $*246$ chart of the *P*, *D* and *G* sur-

faces [Robi 04a], but is not commensurate with the ∗2226 chart of the *H* surface [Robi 04b]. This embedded orbifold is composed of exactly two ∗246 triangles, glued along R_3 (the mirror passing from ∗6 to ∗4). This amalgamated domain has two ∗2 vertices from the original two triangles, an additional ∗2 vertex from a gluing of two ∗4 vertices, and a ∗3 vertex from a gluing of two ∗6 vertices. One fundamental domain of the ∗2223 orbifold embedded in the ∗246 is shown in Fig. 2.20(a).

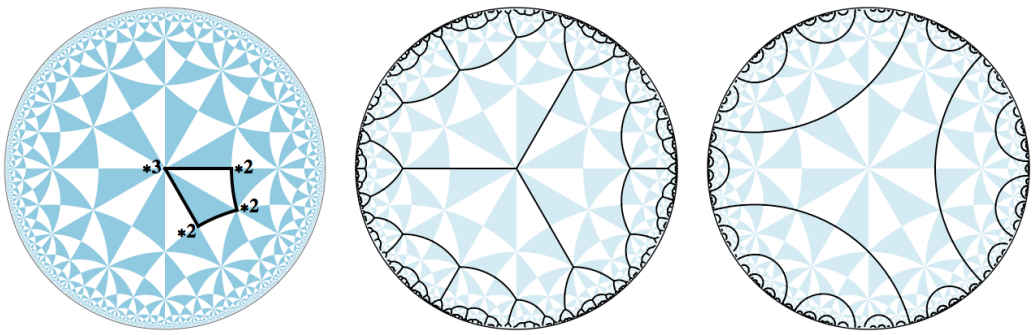

Figure 2.20: (a) The embedding of the ∗2223 orbifold in the ∗246 tiling of $\mathbb{H}^2$: two ∗246 triangles fused along an R_3 boundary. (b) $*246_{124R}$, the embedded regular ribbon tiling of ∗2223. (c) $*246_{124C}$, the embedding of the complementary regular ribbon tiling on ∗2223.

The ∗2223 orbifold has an abstract symmetry (automorphism) along the axis passing from the ∗3 vertex to the opposite ∗2 vertex. Once the orbifold is embedded, however, this abstract symmetry aligns with the R_3 reflection of the ∗246 chart: the automorphism of the orbifold corresponds to a conjugacy of the ∗246 map, so we need only consider one form. The embedded regular ribbon tiling from Fig. 2.18 and the embedding of the complementary tiling represented in Fig. 2.19 are shown in Fig. 2.20(b,c) respectively. The interchange of the tile boundary for the medial axis, the axis of points with more than one closest edge, is apparent. We refer to these embedded tilings by the names $*246_{124R}$ and $*246_{124C}$, symbolising the 124*R* and 124*C* tilings embedded in the ∗246 tiling of $\mathbb{H}^2$.

The orbifold $2*23$ (group 129) contains a 2–fold cone point (the peak of the hat, as shown in Fig. 2.2(b)), with the open brim consisting of two mirrors intersecting each other at two points, one intersection with an angle of $\frac{\pi}{2}$ and the other $\frac{\pi}{3}$. A regular ribbon tiling with a degree–3 vertex and symmetry $2*23$ has an edge passing from the ∗3 site along the mirror boundary to the ∗2 site. This decoration and information can be represented by a Delaney–Dress triangulation of the orbifold (Fig. 2.21), and is called 129*R*. Tiling 129*C* is the complement of this tiling, representing an interchanging of the tile boundaries for the

medial axes. The Delaney–Dress encoding of 129*C* is shown in Fig. 2.22.

Chamber Class	s0	s1	s2	m01	m12
A	**A**	B	**A**	3	9
B	C	**A**	C	3	9
C	B	C	B	3	9

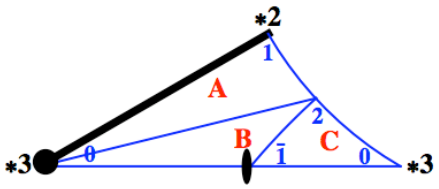

Figure 2.21: The regular ribbon tiling of the $2*23$ orbifold. The decoration passes from the $*3$ site, along the mirror boundary, to the $*2$ site. This tiling is referred to by the label 129*R*.

Chamber Class	s0	s1	s2	m01	m12
A	A	**B**	A	9	3
B	**C**	A	**C**	9	3
C	**B**	**C**	**B**	9	3

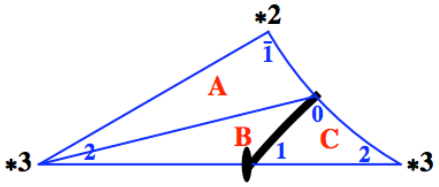

Figure 2.22: The complement of the regular ribbon tiling on $2*23$, 129*C*. The edge passes from the 2–fold rotation to the mirror boundary, incident at right angles. The edge would continue to a copy of the 2–fold rotation in the neighbouring domain.

The $2*23$ orbifold embeds uniquely in $*246$ (Fig. 2.23(a)). The automorphism of the $2*23$ orbifold (an abstract mirror symmetry on the axes passing from the$*3$vertex to the 2–fold rotation) is a conjugacy of the $*246$ tiling: we need only consider a single automorphic embedding of the orbifold. Fig. 2.23(b) and (c) show the embedding of the regular ribbon tiling with $2*23$ symmetry (Fig. 2.21) and the complementary tiling (Fig. 2.22) respectively. We call these two embedded tilings $*246_{129R}$ and $*246_{129C}$, as they are embedded in the $*246$ tiling of $\mathbb{H}^2$.

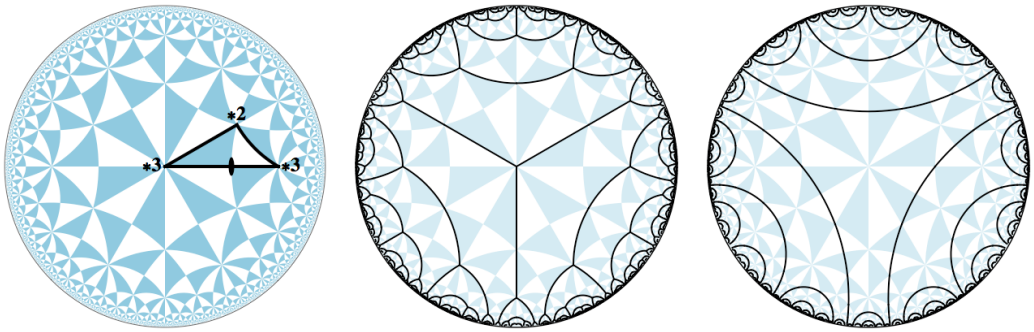

(a) **(b)** **(c)**

Figure 2.23: (a) The unique embedding of the $2*23$ orbifold into the $*246$ tiling of $\mathbb{H}^2$. (b) The embedded regular ribbon tiling with symmetry $2*23$ (Fig. 2.21). (c) The embedded complement of a regular ribbon tiling with symmetry $2*23$ (Fig. 2.22).

A regular ribbon tiling is also supported by the 2223 Stellate orbifold (group 118). The orbifold is decorated by an edge passing from the 3–fold rotation to a 2–fold rotation. Fig. 2.24 shows the regular ribbon tilings tabular representation along with an image of the decorated orbifold, cut open to lay (somewhat) flat. This tiling is referred to as 118*R*. Fig. 2.25 shows the Delaney–Dress representation of the complementary regular ribbon tiling with 2223 symmetry, known as 118*C*.

Chamber Class	s0	s1	s2	m01	m12
A	**D**	B	**D**	4	6
B	C	**A**	C	4	6
C	B	**D**	B	4	6
D	**A**	C	**A**	4	6

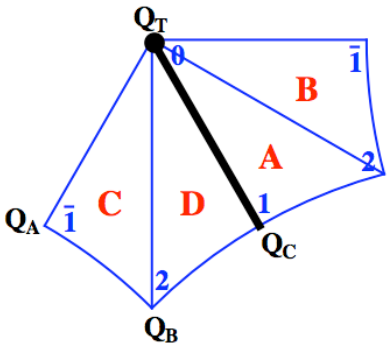

Figure 2.24: Representation of the regular ribbon tiling on the 2223 orbifold. The 2–folds are at Q_A, Q_B and Q_C, the 3–fold is at Q_T. The edge is from Q_T to Q_C.

Chamber Class	s0	s1	s2	m01	m12
A	D	**B**	D	6	4
B	**C**	A	**C**	6	4
C	**B**	D	**B**	6	4
D	A	**C**	A	6	4

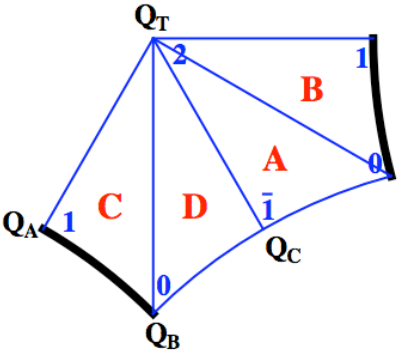

Figure 2.25: Encoding of the complementary regular ribbon tiling on 2223. The 2–folds are at Q_A, Q_B and Q_C, and the 3–fold is Q_T. The edge is from Q_A to Q_B.

The distinct embeddings of the 2223 Stellate orbifold into the $*246$ chart of $\mathbb{H}^2$ discussed in Section 2.2, decorated by the free tilings given in Fig. 2.24 and Fig. 2.25, produce distinct embedded decorations of $\mathbb{H}^2$. The positions of the reference frame generators Q_T, Q_A, Q_B and Q_C in the $*246$ chart are shown in Fig. 2.26. The full fundamental domain, as given in the Delaney–Dress representations of the abstract tilings, may be obtained by doubling the quadrilateral joining the generators across the line joining Q_T and Q_C.

Distinct embeddings of the decorated orbifold into $*246$ directly correspond to embedded parallelograms of unit area in the $\mathbb{Z} \times \mathbb{Z}$ discretisation of $\mathbb{E}^2$. Fig. 2.27 shows two

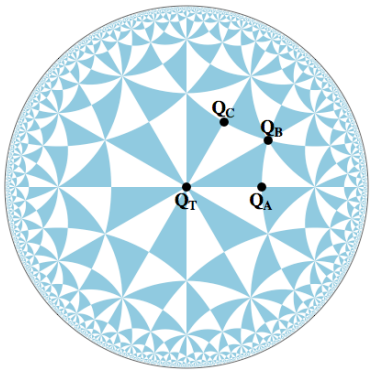

Figure 2.26: The locations of the reference frame generators of the 2223 symmetry group in the $*246$ tiling of $\mathbb{H}^2$.

decorations resulting from the embedding of the 2223 orbifold corresponding to the unit area parallelogram with vertex at the origin, $\{p,q\} = \{0,1\}$ and $\{r,s\} = \{1,0\}$. Additional symmetry is induced in the tiling by the embedding: these tilings have symmetry $*2223$, and are equivalent to those constructed on the $*2223$ orbifold (Fig. 2.20), namely embedded tilings $*246_{124R}$ and $*246_{124C}$.

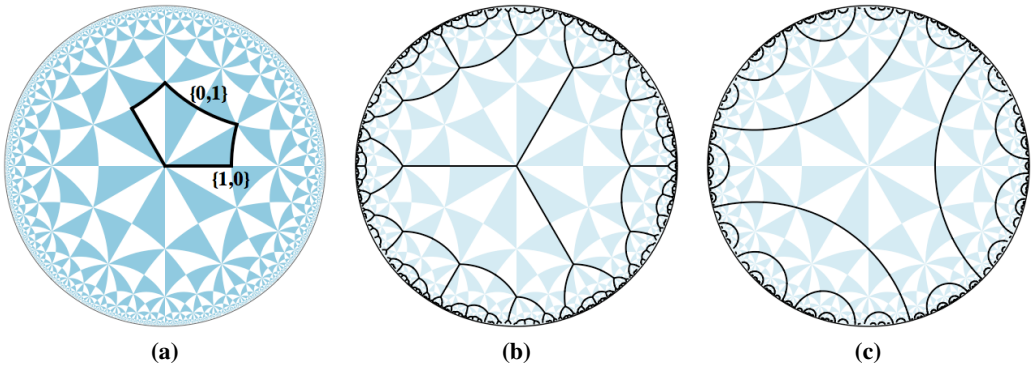

Figure 2.27: (a) An embedded 2223 fundamental domain into $*246$, where Q'_C and Q'_A are located at $\{0,1\}$ and $\{1,0\}$ respectively (see Fig. 2.14 for coordinate grid). This embedding in analogous to a parallelogram in $\mathbb{E}^2$with $\{p,q\}$=$\{0,1\}$ and $\{r,s\}$=$\{1,0\}$. (b) The embedded regular ribbon tiling. (c) The embedded complementary tiling. Both have increased symmetry of $*2223$, equivalent to the tilings shown in Fig. 2.20, namely embedded tilings $*246_{124R}$ and $*246_{124C}$.

Fig. 2.28 shows the decorations resulting from an embedding of the 2223 orbifold indexed by the $\mathbb{E}^2$ parallelogram $\{p,q\} = \{1,1\}$ and $\{r,s\} = \{1,0\}$. Additional symmetry is induced by the embedding, hence these tilings are equivalent to those constructed as decorations of the $2*23$ orbifold (Figs. 2.23), which are embedded tilings $*246_{129R}$ and $*246_{129C}$. Altering the values of r and s for embedded regular ribbon tilings and complements leaves both of the decorations unchanged.

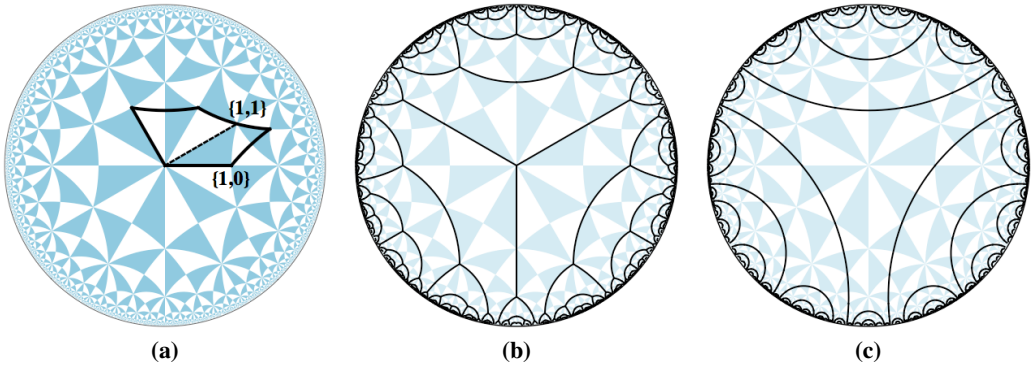

Figure 2.28: (a) An embedding of the 2223 domain into $*246$, where Q'_C and Q'_A are located at $\{1,1\}$ and $\{1,0\}$ respectively. (b) The embedded regular ribbon tiling. (c) The embedded complementary tiling. This embedding has additional symmetries, equivalent to those constructed on the orbifold $2*23$ (Fig. 2.23), namely $*246_{129R}$ and $*246_{129C}$.

For all other embeddings, 2223 will be the maximal symmetry group of the tiling. Where the maximal symmetry of the free tiling is 2223, the free tiling is given the name $*246_{118R}(n)$ or $*246_{118C}(n)$. The variable n ranges from 1 to ∞, and the free tiling is given a value of n based on its relative edge length in $\mathbb{H}^2$: the embedding which has 2223 maximal symmetry and the shortest possible tile edge length of all embeddings will have $n = 1$, the second shortest edge length $n = 2$, *et cetera*. Fig. 2.29 shows example decorations from several embeddings of 2223, indexed by distinct parallelograms of $\mathbb{E}^2$. The three parallelograms, as well as the embedded tiling names are:

1. $\{p,q\} = \{2,1\}$ and $\{r,s\} = \{1,0\}$: $*246_{118R}(1)$ and $*246_{118C}(1)$ (Fig. 2.29(b,c))
2. $\{p,q\} = \{3,1\}$ and $\{r,s\} = \{1,0\}$: $*246_{118R}(2)$ and $*246_{118C}(2)$ (Fig. 2.29(e,f))
3. $\{p,q\} = \{3,2\}$ and $\{r,s\} = \{1,1\}$: $*246_{118R}(3)$ and $*246_{118C}(3)$ (Fig. 2.29(h,i))

As the choice of parallelograms become increasingly oblique (i.e. the tiling approaches $*246_{118R}(\infty)$ and $*246_{118C}(\infty)$), the tilings approach a degenerate case of a set of star graphs with a vertex and three infinite edges in the ribbon tiling case, and a set of asymptotic triangles in the complementary tiling case. Some of these embedded free tilings were studied previously [Hyde 00a]. There are an infinite number of embeddings of the decorated 2223 orbifold into the $*246$ chart of $\mathbb{H}^2$, where these may be indexed by embedded parallelograms of $\mathbb{E}^2$. We have shown the three free tilings which result from the three embeddings with the shortest tile edge lengths in $\mathbb{H}^2$, and the methodology presented may be used to further enumerate all embeddings, if so desired.

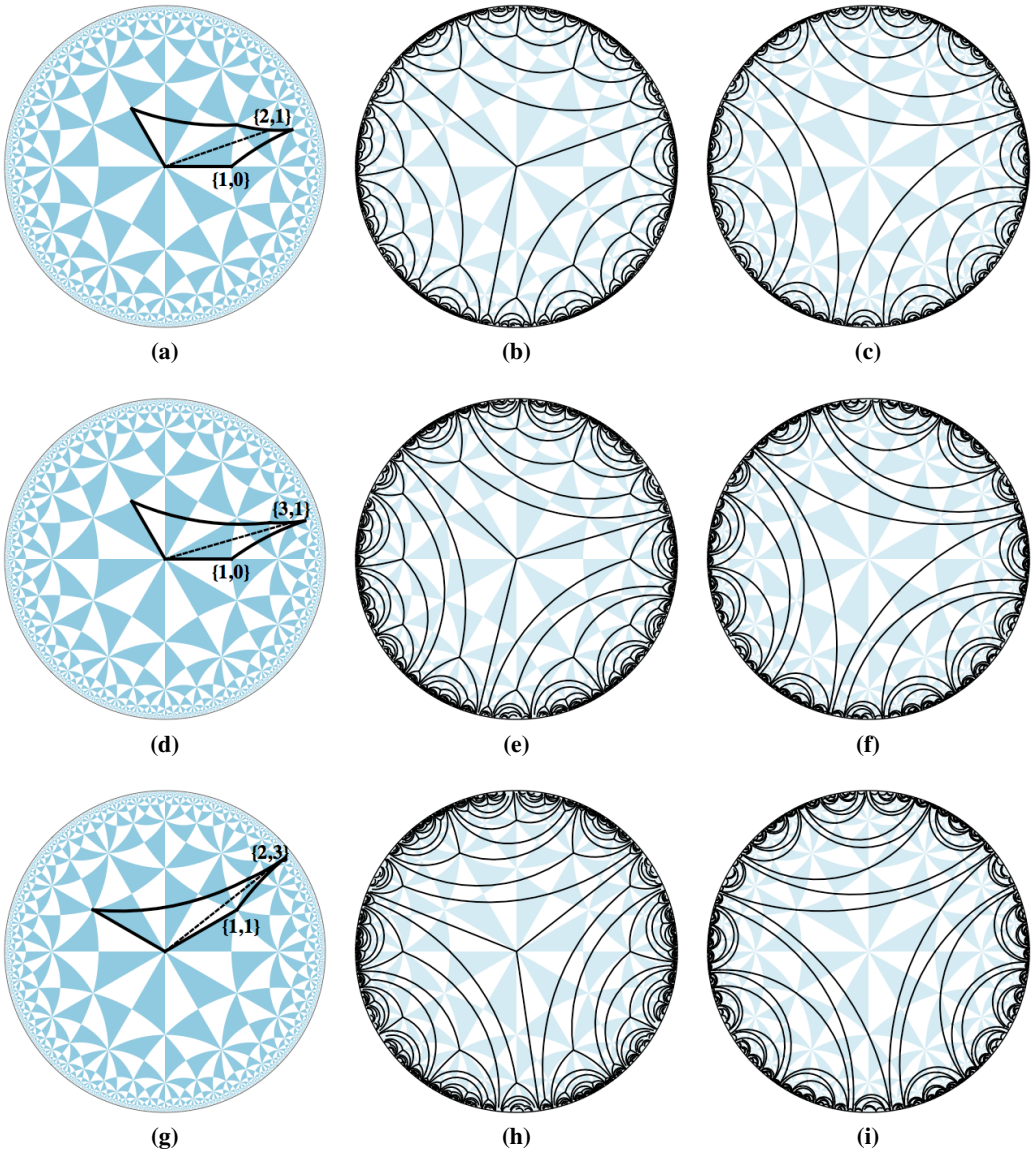

Figure 2.29: Example decorations from several embeddings of 2223. The embedded tiling names are (b) $*246_{118R}(1)$, (c) $*246_{118C}(1)$, (e) $*246_{118R}(2)$, (f) $*246_{118C}(2)$, (h) $*246_{118R}(3)$ and (i) $*246_{118C}(3)$.

The ∗2224 and 2224 symmetry groups permit regular ribbon tilings with degree–4 vertices by a similar construction to the degree–3 tiling case. Regularity and edge–1 transitivity are ensured by a ∗4 junction or 4–fold rotation at the tile vertex, and vertex–1 transitivity by a ∗2 junction or 2–fold rotation at the edge midpoint. The remaining two ∗2 junctions or 2–fold rotations define the translation symmetry of the infinite ribbon tile.

Consider first the ∗2224 orbifold, or group 123 [Robi 04a]. A regular ribbon tiling decorates the ∗2224 orbifold by an edge passing from the ∗4 site, along the mirror boundary, to a ∗2 site. These symmetry components are situated on the infinite boundary components of the tile. The two remaining ∗2 sites of the orbifold define the translation along the interior of the infinite tile. This decoration of the ∗2224 orbifold, known as 123*R*, is shown in Fig. 2.30 along with a table representing the Delaney–Dress encoding of the decorated orbifold.

Chamber Class	s0	s1	s2	m01	m12
A	**A**	B	**A**	4	8
B	B	**A**	B	4	8

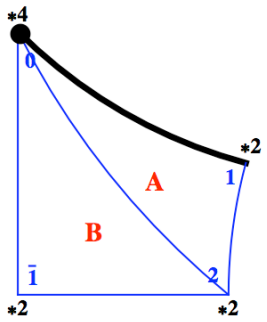

Figure 2.30: Encoding of a regular ribbon tiling on the ∗2224 orbifold, known as 123*R*. The decorations passes from the ∗4 site of the orbifold, along the mirror boundary, to a ∗2 site.

Chamber Class	s0	s1	s2	m01	m12
A	A	**B**	A	8	4
B	**B**	A	**B**	8	4

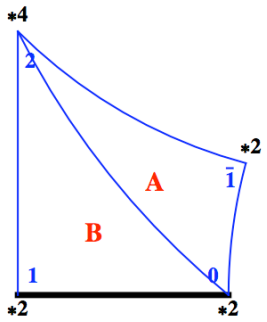

Figure 2.31: Encoding of the complement of a regular ribbon tiling on the ∗2224 orbifold, known as 123*C*. The 0–vertex and 2–vertex sites have been inverted, as well as the 1–vertex and $\bar{1}$–vertex sites. The decoration now passes from a ∗2 site along a mirror boundary to another ∗2 site.

The complement of a regular ribbon tiling on ∗2224 inverts the 0–vertex and 2–vertex sites of the Delaney–Dress triangulation, as well as inverting the 1–vertex and $\bar{1}$–vertex

sites. This exchange of vertices interchanges the boundary of the tile with the axis which is invariant under the internal symmetries of the tile, which is exactly the infinite translation axis of the tile. The Delaney–Dress encoding of the complementary regular ribbon tiling of $*2224$, known as the $123C$ tiling, is shown in Fig. 2.31.

The $*2224$ orbifold may be embedded into the $*246$ chart of the P, D and G surfaces [Robi 04a], but is not commensurate with the $*2226$ chart of the H surface [Robi 04b]. In the process of embedding the orbifold, an automorphism of $*2224$ (along the axis from the $*4$ vertex to the opposite $*2$ vertex) is asymmetrised with respect to the $*246$ tiling. The symmetry breaking induces two geometrically distinct automorphic free tilings for each abstract decoration of the orbifold. Fig. 2.32 shows the $*2224$ orbifold embedded in the $*246$ tiling of $\mathbb{H}^2$, as well as two automorphic regular ribbon tilings (represented in Fig. 2.30), and the two complementary tilings (represented in Fig. 2.31). We label these embedding $*246_{123R}(n)$ and $*246_{123C}(n)$, where n takes the value of 1 for the embedding with the shorter edge length, and 2 for the embedding with the longer edge length.

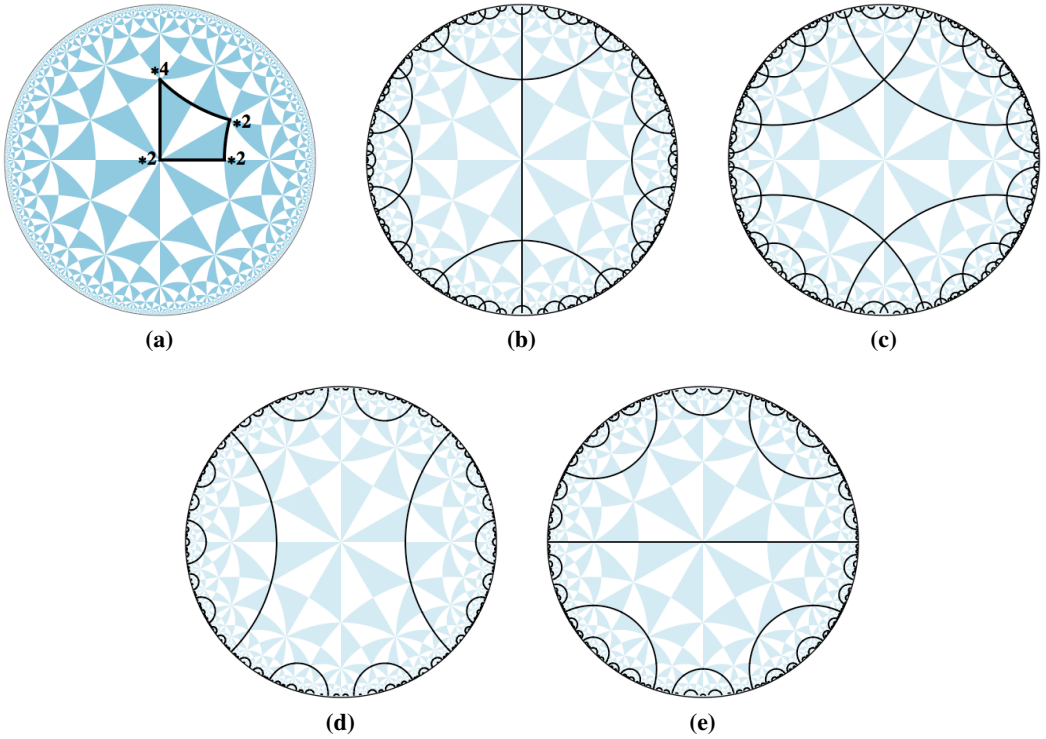

Figure 2.32: (a) Embedding of the $*2224$ orbifold into the $*246$ tiling, where the abstract symmetry of the orbifold is now asymmetrised. (b,c) Two automorphic regular ribbon tilings (Fig. 2.30), titled $*246_{123R}(1)$ and $*246_{123R}(2)$ respectively. (d,e) Two automorphic complementary tilings (Fig. 2.31), which are known as $*246_{123C}(1)$ and $*246_{123C}(2)$ respectively.

We note that the $2*24$ orbifold is not a member of the quotient group $*246/\circ\circ\circ$, and hence we do not consider regular ribbon tilings or their complements constructed on this symmetry group. In general, however, this orbifold will support such regular ribbon tilings, and may be constructed as per the $2*23$ regular ribbon tilings.

A regular ribbon tiling decorates the 2224 orbifold, group 114 [Robi 04a], by an edge passing from the 4–fold rotation to a 2–fold rotation. Fig. 2.33 shows the tabular representation of this decoration, along with a decorated image of the orbifold. This tiling is known as 114*R*, as it the regular ribbon tiling of group 114.

Chamber Class	s0	s1	s2	m01	m12
A	**D**	B	**D**	4	8
B	C	**A**	C	4	8
C	B	**D**	B	4	8
D	**A**	C	**A**	4	8

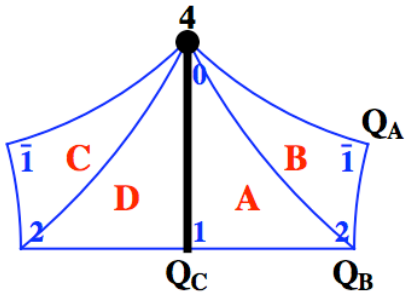

Figure 2.33: A regular ribbon tiling on the 2224 orbifold, known as 114*R*. The decoration passes from the 4–fold rotation to the 2–fold rotation labelled Q_C.

Exchanging the tile boundary with the infinite translation axis of the tile gives a complementary free tiling. Fig. 2.25 shows the encoding of this complementary regular ribbon tiling, the 114*C* tiling, which has the decorative edge passing between two distinct 2–fold rotations.

Chamber Class	s0	s1	s2	m01	m12
A	D	**B**	D	8	4
B	**C**	A	**C**	8	4
C	**B**	D	**B**	8	4
D	A	**C**	A	8	4

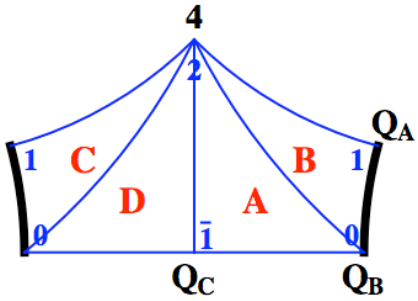

Figure 2.34: The complement to the regular ribbon tiling on the 2224 orbifold domain, also known as 114*C*. The decoration passes between the 2–fold rotations labelled Q_A and Q_B.

We index $\mathbb{H}^2$ embeddings of the 2224 orbifold by embedded parallelograms of $\mathbb{E}^2$, as is the case for all 222k orbifolds. A quadrant of $\mathbb{E}^2$ embeds in a $\frac{\pi}{4}$ sector of the 2224 discretisation of $\mathbb{H}^2$(Fig. 2.35(a)). The embedded quadrant has both coordinates positive, and

passing to adjacent $\frac{\pi}{4}$ sectors of the 2224 discretisation yields distinctly signed quadrants of $\mathbb{E}^2$.

The reference frame embedding of the generators of the 2224 orbifold into the $*246$ tiling of $\mathbb{H}^2$ is set (Fig. 2.35(b)). A fundamental domain (equivalent to that which is shown in the Delaney–Dress encoding) may be obtained by doubling the quadrilateral formed by the generating elements across the line joining Q_T and Q_C. Distinct free tilings result from the choice of embedded unit parallelograms in the $\mathbb{Z}\times\mathbb{Z}$ grid of $\mathbb{E}^2$.

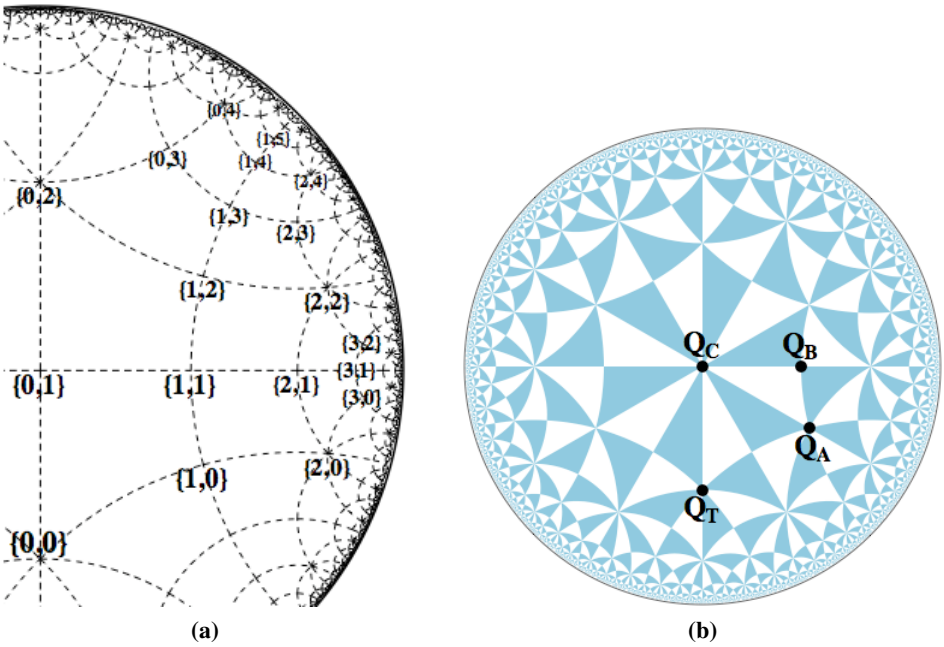

Figure 2.35: (a) Coordinates of the grid $\mathbb{Z}\times\mathbb{Z}$ within the 2224 discretisation of $\mathbb{H}^2$. (b) The reference frame generators within the $*246$ tiling of $\mathbb{H}^2$.

Mirrors are inherent in the geometry when embedding the parallelograms $\{p,q\}=\{0,1\}$, $\{r,s\}=\{1,0\}$ and $\{p,q\}=\{1,0\}$, $\{r,s\}=\{0,1\}$ into the 2224 discretisation of $\mathbb{H}^2$. This results in tilings with $*2224$ symmetry, equivalent to the $*246_{123R}(1)$, $*246_{123R}(2)$, $*246_{123C}(1)$ and $*246_{123C}(2)$ embedded tilings, as constructed on the $*2224$ orbifold (Fig. 2.32).

The regular ribbon tilings and complementary tilings that result from the embedding of some Euclidean parallelograms into the 2224 discretisation of $\mathbb{H}^2$ are given as examples (Fig. 2.36). We name these embedded tilings $*246_{114R}(n)$ for regular ribbon tilings and $*246_{114C}(n)$ for their complements, where n counts from smallest edge length (by hyperbolic length) within the embedded fundamental domain upwards through all possi-

ble embeddings. The Euclidean parallelograms defining the embeddings, as well as their embedded tiling names, are given by:

1. $\{p,q\} = \{1,1\}$ and $\{r,s\} = \{1,0\}$: $*246_{114R}(1)$ and $*246_{114C}(1)$ (Fig. 2.36(b,c))
2. $\{p,q\} = \{1,2\}$ and $\{r,s\} = \{1,1\}$: $*246_{114R}(2)$ and $*246_{114C}(2)$ (Fig. 2.36(e,f))
3. $\{p,q\} = \{2,1\}$ and $\{r,s\} = \{1,0\}$: $*246_{114R}(3)$ and $*246_{114C}(3)$ (Fig. 2.36(h,i))

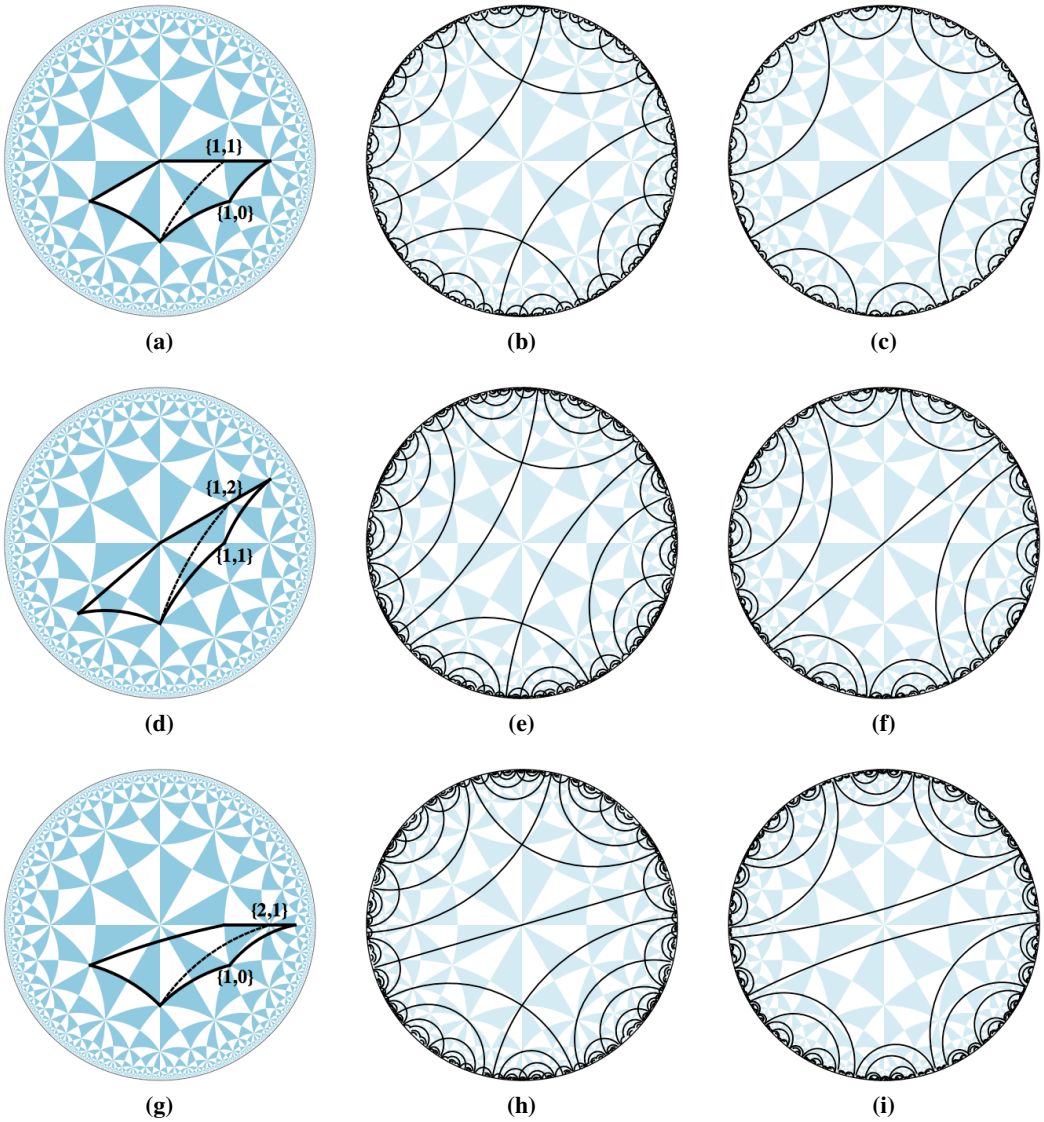

Figure 2.36: Example decorations from several embeddings of 2224. Their embedded tiling names are (b $*246_{114R}(1)$, (c) $*246_{114C}(1)$, (e) $*246_{114R}(2)$, (f) $*246_{114C}(2)$, (h) $*246_{114R}(3)$, (i) $*246_{114C}(3)$.

Tilings with 5–fold regular symmetry are not compatible with either the ∗246 or the ∗2226 tiling, hence we disregard these cases. Regular ribbon tilings with 6–fold symmetry at the tile vertex may have symmetry ∗2226, 2∗26, 2226 or 26×. Regular ribbon tilings on the 26× orbifold always have increased symmetry of 2∗26, hence we disregard decorations of this orbifold. The ∗2226 symmetry group is in the ∗2226/○○○ quotient group, the 2∗26 symmetry group is in the ∗246/○○○ quotient group, and the 2226 symmetry group is in both of the ∗246/○○○ and ∗2226/○○○ quotient groups.

A regular ribbon tiling reticulates the ∗2226 orbifold, which is group 32 of the ∗2226/○○○ quotient group [Robi 04b], by passing from the ∗6 site, along a mirror boundary, to a ∗2 site (Fig. 2.37). These symmetry elements, to which the decoration is incident, generate the boundary components of the infinite tile. The set of parallel mirrors contained within the two remaining ∗2 sites generate the single internal translation of the infinite ribbon tile. This tiling is known as 32*R*, as it is the regular ribbon tiling of group 32 in the ∗2226/○○○ quotient group.

Chamber Class	s0	s1	s2	m01	m12
A	**A**	B	**A**	4	12
B	B	**A**	B	4	12

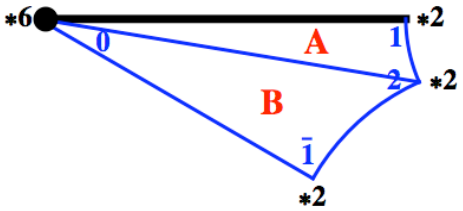

Figure 2.37: A regular ribbon tiling represented as a decoration on the ∗2226 orbifold, passing from the ∗6 site, along a mirror boundary, to a ∗2 site. This tiling is known as the 32*R* tiling.

The complement of the regular ribbon tiling exchanges the infinite translation axis of the infinite ribbon tile with the boundary components of the tile. On the ∗2226 orbifold, this complementary tiling can be represented by a decorative edge passing from a ∗2 site, along a mirror boundary, to another ∗2 site of the orbifold. This tiling, known as 32*C*, is encoded in Fig. 2.38.

Chamber Class	s0	s1	s2	m01	m12
A	A	**B**	A	12	4
B	**B**	A	**B**	12	4

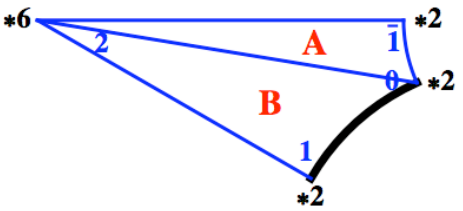

Figure 2.38: The complement to the regular ribbon tiling on the ∗2226 orbifold. The decoration passes from a ∗2 site, along a mirror boundary, to another ∗2 site. This tiling as known as the 32*C* tiling.

The $*2226$ orbifold is precisely the $*2226$ chart of $\mathbb{H}^2$ inherited from the H surface. The orbifold has an abstract symmetry (automorphism) that swaps the two $*2$ vertices adjacent to the $*6$ corner. This abstract symmetry is broken by the embedding of the $*2226$ domain into $\mathbb{H}^2$ (by the free parameter of the H surface discussed previously), and hence the automorphic tilings have distinct geometries in the $*2226$ chart. Fig. 2.39 shows the embedded fundamental domain of the $*2226$ orbifold, along with the four free tilings of this symmetry group (two automorphic versions of the regular ribbon tiling, and two of the complementary tiling, all with symmetry $*2226$). These embedded tilings are named to reflect their embedding into the $*2226$ tiling of $\mathbb{H}^2$: hence they are named $*2226_{32R}(1)$, $*2226_{32R}(2)$, $*2226_{32C}(1)$ and $*2226_{32C}(2)$, where the '1' refers to a shorter edge length in one asymmetric domain.

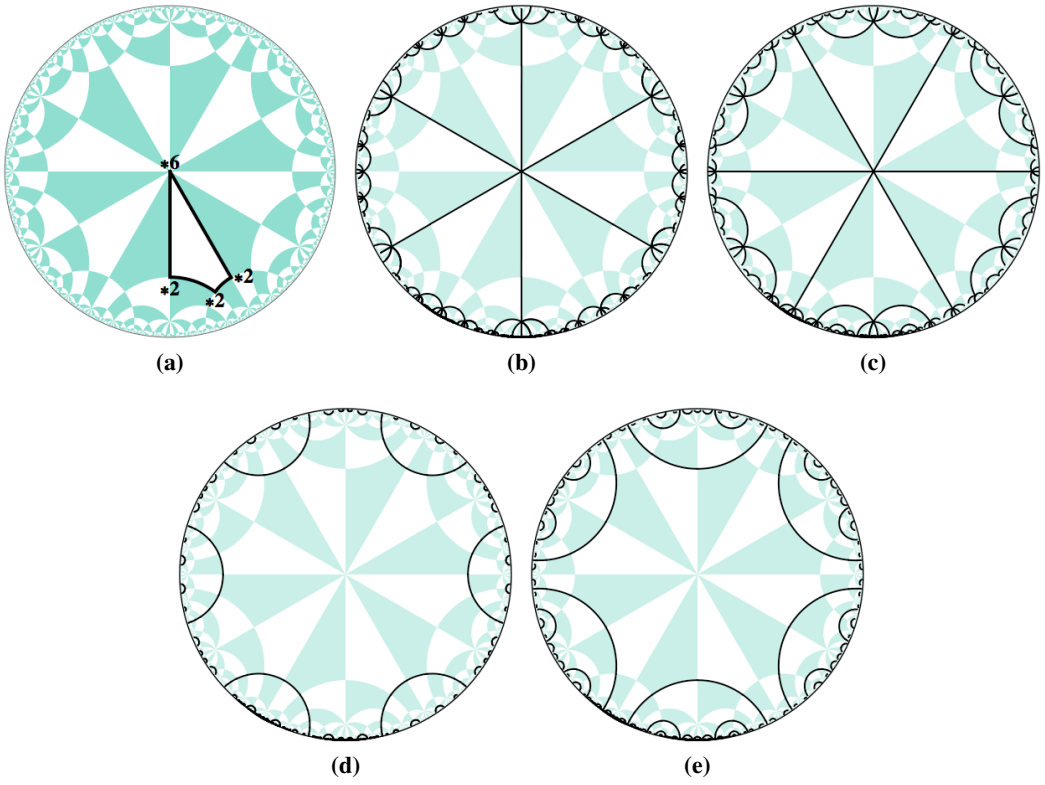

Figure 2.39: (a) A fundamental domain of the $*2226$ orbifold uniquely embedded into the $*2226$ tiling of $\mathbb{H}^2$. (b,c) Two automorphic regular ribbon tilings on the $*2226$ orbifold, known as $*2226_{32R}(1)$ and $*2226_{32R}(2)$. (d,e) Two automorphic versions of the complementary tiling on the $*2226$ orbifold, namely $*2226_{32C}(1)$ and $*2226_{32C}(2)$.

We treat the $2*26$ orbifold equivalently to the $2*23$ orbifold considered previously. We construct two simple orbifold decorations: an edge passing from the $*6$ vertex to the $*2$ vertex to give the regular ribbon tilings on this orbifold, and the complementary

tiling having an edge passing from the 2–fold rotation, through a mirror boundary at right angles, to an image of the same 2–fold rotation. The topology of these two tilings, named 122*R* and 122*C*, are abstractly represented by the two Delaney–Dress symbols given in Figs. 2.40 and 2.41.

Chamber Class	s0	s1	s2	m01	m12
A	**A**	B	**A**	3	18
B	C	**A**	C	3	18
C	B	C	B	3	18

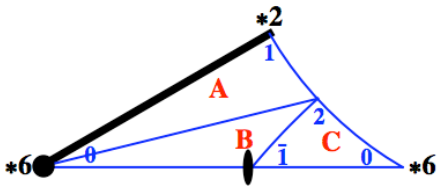

Figure 2.40: Encoding of the topology of a regular ribbon tiling on the $2*26$ orbifold: 122*R* The decoration consists of an edge passing from the $*6$ site, along the mirror boundary to the $*2$ site.

Chamber Class	s0	s1	s2	m01	m12
A	A	**B**	A	18	3
B	**C**	A	**C**	18	3
C	**B**	**C**	**B**	18	3

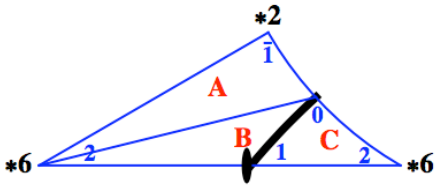

Figure 2.41: Encoding of the topology of a complementary regular ribbon tiling on the $2*26$ orbifold: 122*C*. The decoration consists of an edge passing from the 2–fold rotation to an image of itself through a mirror boundary.

Fig. 2.42(a) shows the unique embedding of the $2*26$ orbifold into the $*246$ chart of $\mathbb{H}^2$. The automorphism of the orbifold $2*26$ is a symmetry line passing from the $*2$ vertex to the 2–fold rotation, mapping the $*6$ site to the other $*6$ site in the embedding. This symmetry is broken with respect to the $*246$ chart when the orbifold is embedded, hence we consider both geometries that arise from automorphic embeddings. Fig. 2.42(b,c) show the two automorphic regular ribbon tilings with distinct geometry that arise from the embedding of the 122*R* tiling (Fig. 2.40) in the $*246$ chart of $\mathbb{H}^2$. These embedded tilings are symbolised by $*246_{122R}(1)$ and $*246_{122R}(2)$ respectively, where the former has a shorter edge length in the asymmetric domain. Fig. 2.42(d,e) also shows the two automorphic complementary tilings given by the embedding of the 122*C* tiling (Fig. 2.41). These tilings are called $*246_{122C}(1)$ and $*246_{122C}(2)$ respectively.

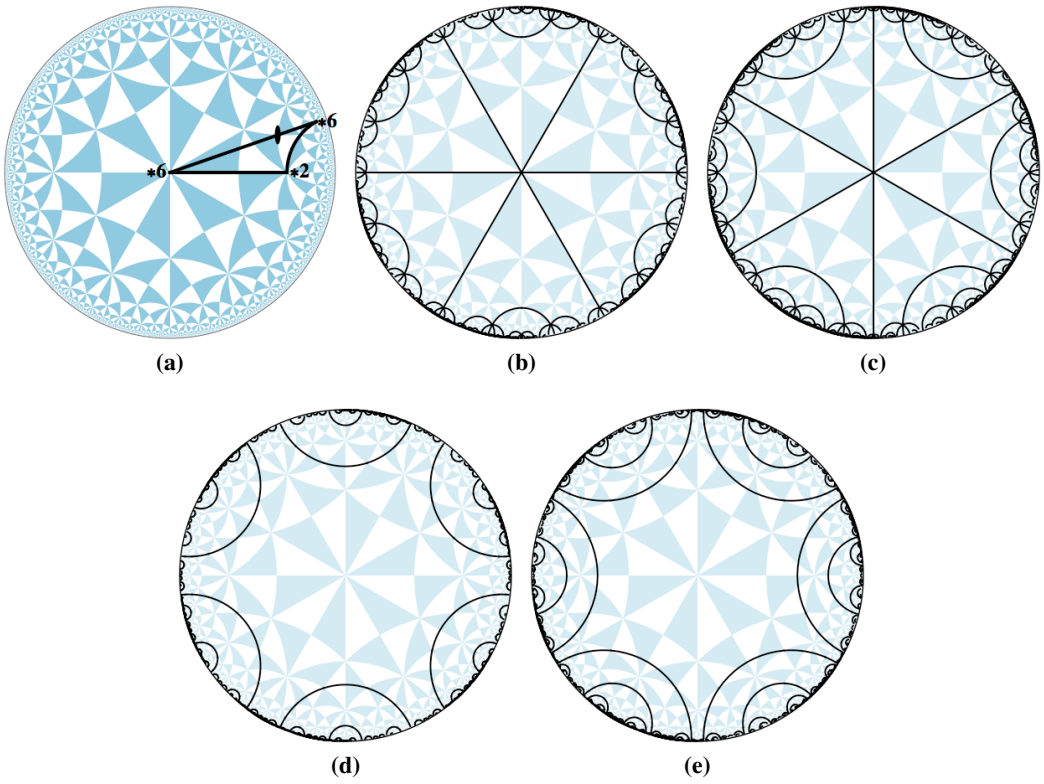

Figure 2.42: (a) Unique embedding of the $2*26$ orbifold into the $*246$ chart of $\mathbb{H}^2$. (b,c) The two automorphic regular ribbon tilings resulting embedding of the $2*26$ domain, namely $*246_{122R}(1)$ and $*246_{122R}(2)$. (d,e) The two automorphic complementary tilings called $*246_{122C}(1)$ and $*246_{122C}(2)$.

A regular ribbon tiling is constructed on the 2226 orbifold (group 31 in ∗2226/○○○ or group 93 in ∗246/○○○ [Robi 04b, Robi 04a]) by an edge passing from the 6–fold rotation to any 2–fold rotation. Fig. 2.43 shows the Delaney–Dress representation of this decoration, and an image of the decorated orbifold. We call this tiling either 31*R* where it may be embedded in the ∗2226 tiling, or 93*R* for embedding in ∗246. The exchange of the tile boundary with the medial axis gives the complementary tiling, whose Delaney–Dress encoding is sown in Fig. 2.44. This tiling is called 31*R* for ∗2226 embeddings or 93*R* for ∗246 embeddings.

Chamber Class	s0	s1	s2	m01	m12
A	**D**	B	**D**	4	12
B	C	**A**	C	4	12
C	B	**D**	B	4	12
D	**A**	C	**A**	4	12

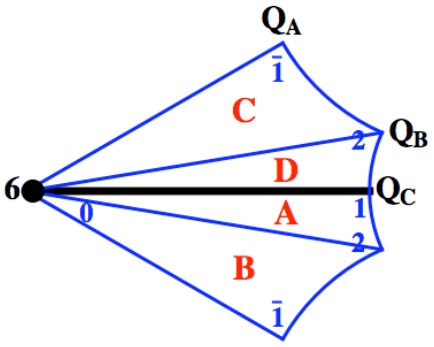

Figure 2.43: Encoding of the regular ribbon tiling on 2226, having the decoration passing from the 6–fold rotation to the 2–fold rotation marked Q_C. We call this tiling either 31*R* where it may be embedded in the ∗2226 tiling, or 93*R* for embedding in ∗246.

Chamber Class	s0	s1	s2	m01	m12
A	D	**B**	D	12	4
B	**C**	A	**C**	12	4
C	**B**	D	**B**	12	4
D	A	**C**	A	12	4

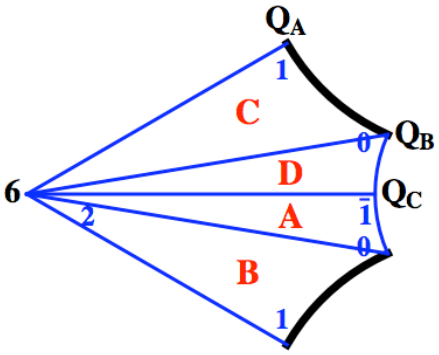

Figure 2.44: Encoding of the complement of the regular ribbon tiling on 2226. The decoration passes between the 2–fold rotations marked Q_A and Q_B. This tiling is called 31*R* for ∗2226 embeddings or 93*R* for ∗246 embeddings.

The 2226 orbifold is commensurate with both of the ∗246 and ∗2226 tilings, and can be mapped onto the *P*, *D*, *G* and *H* surfaces. To assign geometry commensurate with the surfaces, we utilise parallelograms embedded in $\mathbb{E}^2$ to embed the orbifold into $\mathbb{H}^2$ given a specific reference frame (Section 2.2). The positions of the reference frame generators for

the 2226 symmetry group in the ∗2226 and ∗246 tilings are shown in Fig. 2.45.

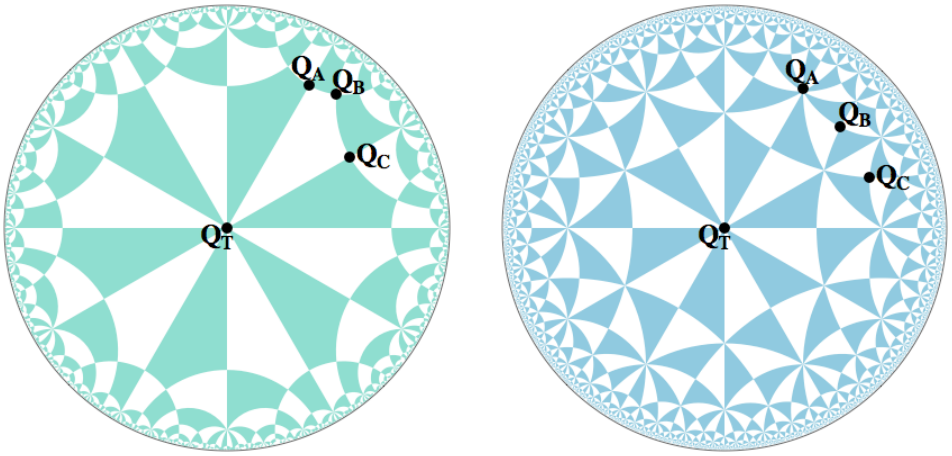

Figure 2.45: The reference frame generators for the 2226 symmetry group in the (a) ∗2226 and (b) ∗246 tilings. To establish an integer grid, Q_A, Q_B and Q_C are located at {0,1}, {1,1} and {1,0} respectively.

We embed the abstract decorations of 2226, tilings $31R$ and $31C$, into the ∗2226 chart of $\mathbb{H}^2$. This process specifies three generators of the 2226 symmetry group relative to the reference frame embedding, and the full fundamental domain is found by doubling the quadrilateral formed across the line connecting Q_T–Q_C. To achieve this embedding, we specify a $\{p,q\}$ and $\{r,s\}$ value in $\mathbb{Z}\times\mathbb{Z}$, where $\{p,q\}$ designates the position of Q_C and $\{r,s\}$ designates the position of Q_A. The geometry inherited from embedding the parallelograms $\{p,q\}=\{0,1\}$ and $\{r,s\}=\{1,0\}$, as well as $\{p,q\}=\{1,0\}$ and $\{r,s\}=\{0,1\}$ have mirror symmetry present, giving a tiling with ∗2226 symmetry. These embedded tilings are equivalent to those constructed on the ∗2226 orbifold (Fig. 2.39), called $*2226_{32R}(1)$, $*2226_{32R}(2)$, $*2226_{32C}(1)$ and $*2226_{32C}(2)$.

Fig. 2.46 shows three examples of embedded regular ribbon tilings and complementary tilings, where the maximal symmetry is 2226. The embedding of the 2226 domain in the ∗2226 tiling of $\mathbb{H}^2$ is inherited from parallelograms in $\mathbb{E}^2$. We give their parallelogram coordinates and embedded tiling names:

1. $\{p,q\}=\{1,1\}$ and $\{r,s\}=\{0,1\}$: $*2226_{31R}(1)$ and $*2226_{31C}(1)$ (Fig. 2.46(b,c))
2. $\{p,q\}=\{2,1\}$ and $\{r,s\}=\{1,1\}$: $*2226_{31R}(2)$ and $*2226_{31C}(2)$ (Fig. 2.46(e,f))
3. $\{p,q\}=\{1,2\}$ and $\{r,s\}=\{0,1\}$: $*2226_{31R}(3)$ and $*2226_{31C}(3)$ (Fig. 2.46(h,i))

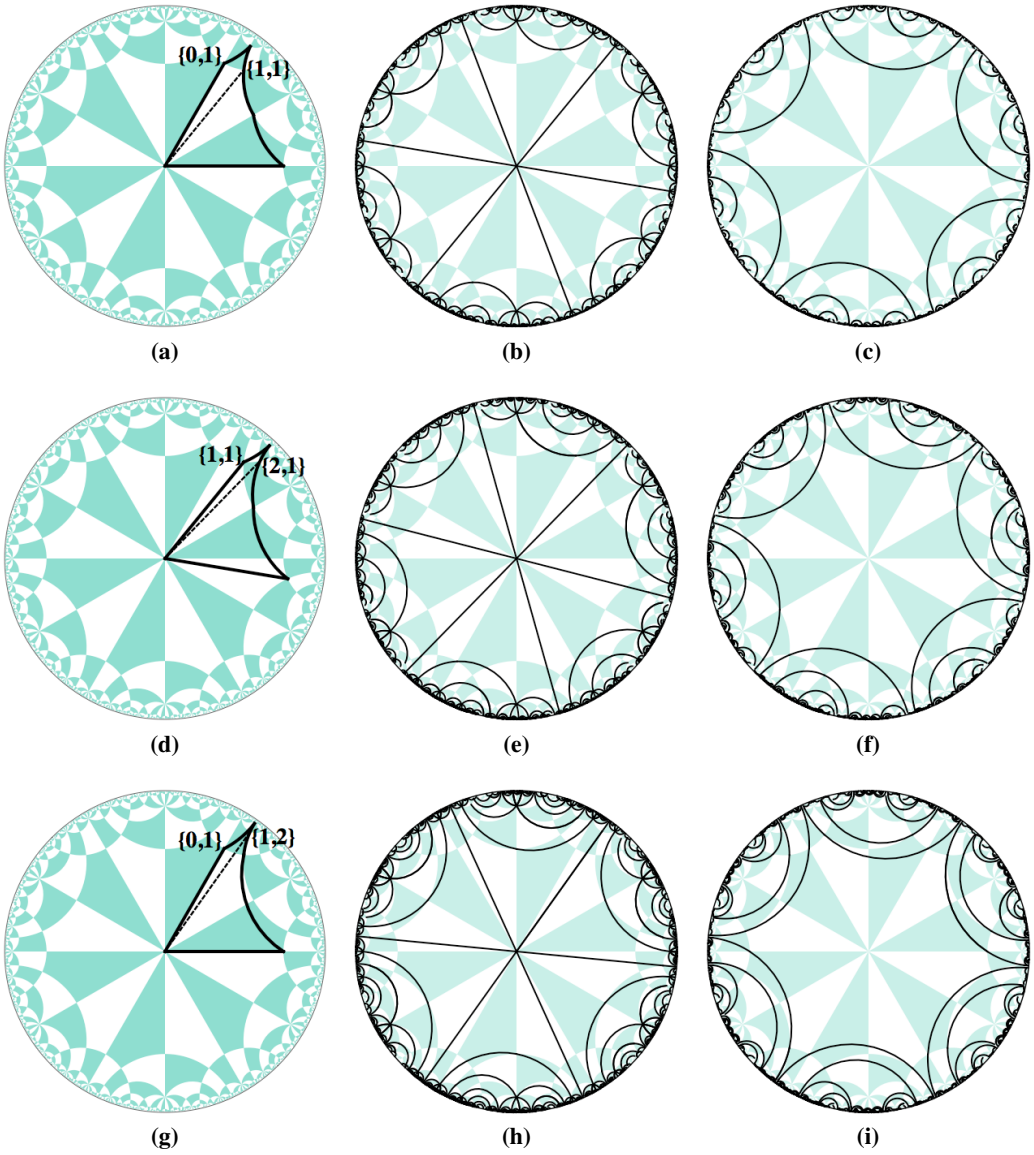

Figure 2.46: Example decorations from embedding 2226 into the $*2226$ chart of $\mathbb{H}^2$. (b) $*2226_{31R}(1)$, (c) $*2226_{31C}(1)$, (e) $*2226_{31R}(2)$, (f) $*2226_{31C}(2)$, (h) $*2226_{31R}(3)$, (i) $*2226_{31C}(3)$.

We now consider embeddings of the $93R$ and $93C$ into the $*246$ chart of $\mathbb{H}^2$. The embedding associated with $\{p,q\} = \{0,1\}$ and $\{r,s\} = \{1,0\}$ (recall that $\{p,q\}$ always specifies the Q_C value), as well as the embedding $\{p,q\} = \{2,1\}$ and $\{r,s\} = \{1,1\}$ will give an increase of symmetry of the pattern to $2*26$, which are the tilings $*246_{122R}(1)$, $*246_{122R}(2)$, $*246_{122C}(1)$ and $*246_{122C}(2)$, as seen in Fig. 2.42.

Fig. 2.47 shows two examples of embedded regular ribbon and complementary tilings into the $*246$ chart. The embeddings used for these tilings correspond to the parallelograms in $\mathbb{E}^2$ with coordinates, and embedded tiling names, as follows:

1. $\{p,q\} = \{1,1\}$ and $\{r,s\} = \{0,1\}$: $*246_{93R}(1)$ and $*246_{93C}(1)$ (Fig. 2.47(b,c))
2. $\{p,q\} = \{1,2\}$ and $\{r,s\} = \{0,1\}$: $*246_{93R}(2)$ and $*246_{93C}(2)$ (Fig. 2.47(e,f))

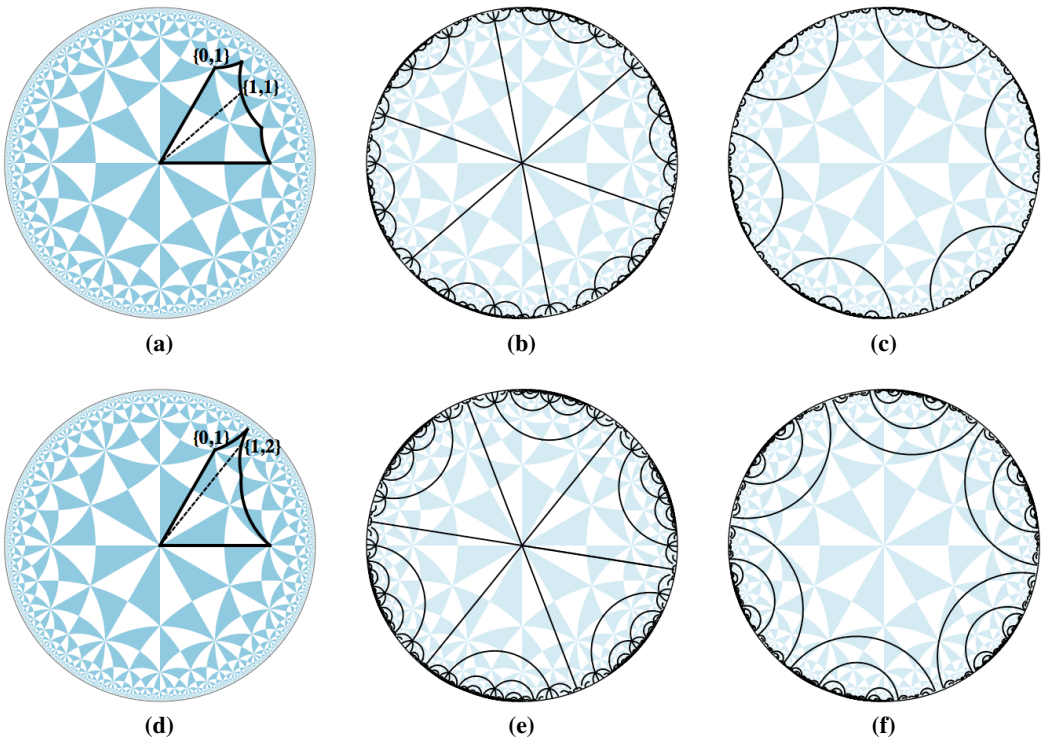

Figure 2.47: Example decorations from several embeddings of 2226 into the $*246$ chart of $\mathbb{H}^2$, indexed by distinct parallelograms (a–c) $\{p,q\} = \{1,1\}$ and $\{r,s\} = \{0,1\}$, known as $*246_{93R}(1)$ and $*246_{93C}(1)$, (d–f) $\{p,q\} = \{1,2\}$ and $\{r,s\} = \{0,1\}$, known as $*246_{93R}(2)$ and $*246_{93C}(2)$.

These cases cover some examples of the embedding of regular ribbon tilings commensurate with the genus–3 TPMS chosen, the regular ribbon tiling supported only by orbifolds of the form 222k. We have, however, provided a method for indexing of possible embeddings of orbifolds of this form (222k), regardless of the orbifold decoration.

2.4 Lower Order Symmetry Groups

An indexing by Euclidean parallelograms has been possible for all of the embedded orbifolds presented so far. A simple extension of this indexation includes a slightly broader set of orbifolds: those where we may index embeddings by gluing distinct Euclidean parallelograms across an edge. This surgery enables indexation of stellate orbifolds of the type 2222j. We explain this construction, and then present examples of embedded 22223 orbifolds with a specific decoration.

A 2222j orbifold is double the size of a 222k orbifold for $k = 2j$, by the orbifold 'cost' formula (Section 2.0.1): 22223 is twice the area of 2226. An embedded 2222j domain may be constructed by taking a 222k symmetry group and doubling across an edge, where the k–fold rotation halves (becoming a j–fold rotation), one 2–fold rotation is deleted, and two copies of the remaining two 2–fold rotations give the four 2–fold rotations of 2222j. These embedded 2222j domains form a subset of the possible embeddings of the domain, and we extend here to encompass all possible embedded domains.

To construct a 22222 domain using multiple 2224 domains ($j = 2$, $k = 2j = 4$), we begin with a $\frac{\pi}{4}$ sector of $\mathbb{H}^2$ discretised by 2224 and the $\mathbb{Z} \times \mathbb{Z}$ grid. We then:

1. Set an origin. This will be a 4–fold rotation of 2224, and will end up as a 2–fold rotation of the 22222 symmetry group.

2. Select Q'_C (or $\{p,q\}$) as a coprime in the $\mathbb{Z} \times \mathbb{Z}$ grid.

3. Select any Q'_A ($\{r_1,s_1\}$ in this case) such that $ps_1 - qr_1 = 1$. The result is a unit parallelogram that embeds as a 2224 quadrilateral, located on a specific side of Q'_C.

4. Select any Q''_A (called $\{r_2,s_2\}$) such that $ps_2 - qr_2 = -1$. This is a quadrilateral that sits on the opposite side of the Q'_C edge to the first constructed quadrilateral.

5. When the the symmetry element Q'_C is discarded and the symmetry of the 4–fold rotation is reduced to a 2–fold rotation, the remaining five 2–fold rotations define an embedded 22222 symmetry group. This process is shown in Fig. 2.48.

When embedding the 22222 domain into $*246$, we are embedding it into the 2224 reference frame. Hence there are three distinct infinite sets of 2–fold rotations, which correspond to the images of each of the three distinct 2–fold rotations of 2224. These three distinct sets are categorised by the 2–fold rotations which lie at $*6$ sites, $*4$ sites and $*2$

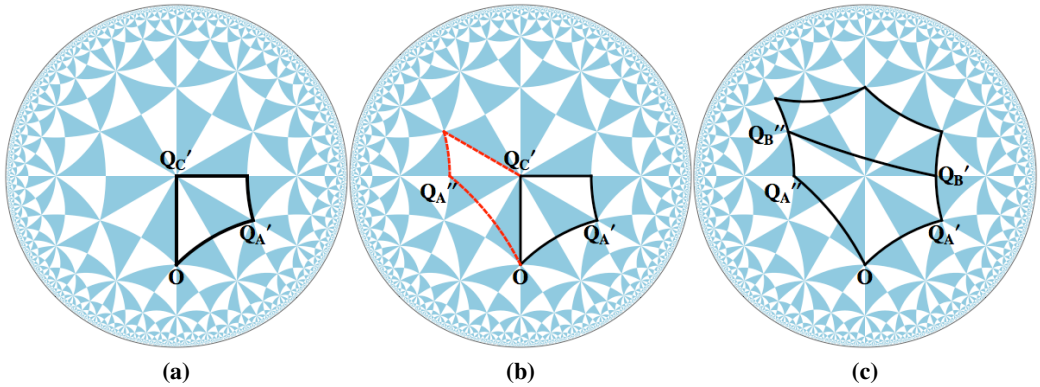

Figure 2.48: (a) Q'_C (or $\{p,q\}$) is the coprime pair $\{0,1\}$ in the $\mathbb{Z}\times\mathbb{Z}$ grid, and Q'_A ($\{r_1,s_1\}$) is the point $\{1,0\}$, where $ps_1 - qr_1 = (0) - (1) = -1$. This parallelogram embeds as a 2224 quadrilateral. (b) Q''_A ($\{r_2,s_2\} = \{-1,1\}$) is selected such that $ps_2 - qr_2 = (0) - (-1) = 1$. This gives a quadrilateral on the opposite side of Q'_C. (c) When Q'_C is discarded, the 4–fold reduced to a 2–fold, and the remaining 2–fold rotations define 22222.

sites respectively. By choosing Q'_C from a particular set of 2–fold rotations, we designate which set of 2–fold rotations will not be isometries of the 22222 embedding. Thus there are three embeddings of the 22222 orbifold with distinct generators, as described in [Robi 04a].

Chamber Class	s0	s1	s2	m01	m12
A	A	**B**	A	8	4
B	**C**	A	**B**	8	4
C	**B**	D	**C**	8	6
D	D	**C**	D	8	6

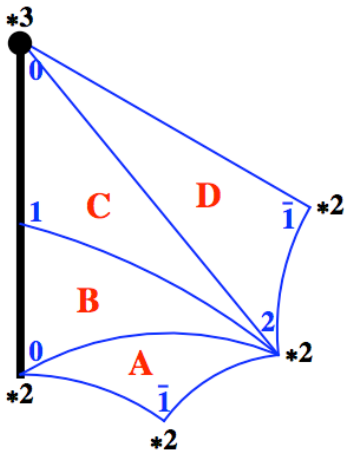

Figure 2.49: The Delaney–Dress symbol for the ∗22223 orbifold decoration having one edge pass from the ∗3 vertex along the mirror boundary to a ∗2 vertex, called 26*R* A visual representation of the decoration and chambers on the orbifold is also shown.

More generally, the 4–fold vertex in the example that has been constructed may be any even number of rotations, thus an equivalent construction will work for any 2222j orbifold. The examples we wish to analyse with this construction are the symmetry groups ∗22223 (group 26 in ∗2226/○○○) and 22223 (group 22 in ∗2226/○○○ and group 49 in

$*246/\circ\circ\circ$). Consider free tilings that are regular (1–transitive edges), and the infinite tiles are branched rather than ribbons. These branched tiles induce vertices in the complementary tiles, rather than infinite geodesic boundaries in the case of ribbon tilings, and we omit these complementary tilings. The Delaney–Dress representation of the decoration of the $*22223$ domain is given in Fig. 2.49: as a decoration of the orbifold, this tiling is called $26R$.

There is one embedding of this orbifold into the $*2226$ domain that is commensurate with the translational symmetries of the H surface ($\circ\circ\circ$) [Robi 04b]. This embedding and the resulting embedded free tiling is shown in Fig. 2.50. This embedded tiling is called $*2226_{26R}$.

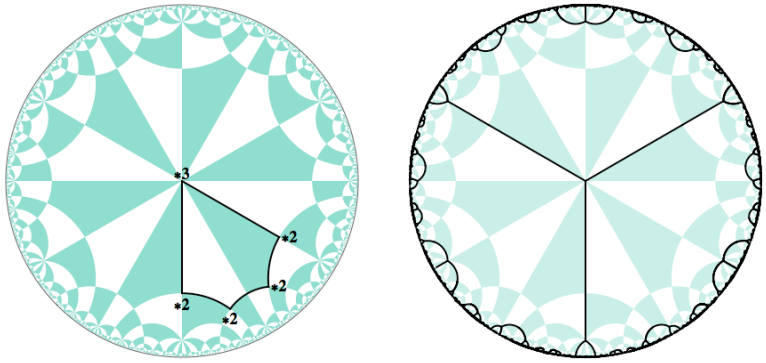

Figure 2.50: (a,b) One embedding of the $*22223$ domain into the $*2226$ tiling of $\mathbb{H}^2$, and the resulting free tiling: $*2226_{26R}$.

The only regular free tiling of the 22223 orbifold is shown in Fig. 2.51, having a single edge passing from the 3–fold rotation to the 2–fold rotation called Q_E. This abstract decoration of the orbifold is called $22R$ as a member of the $*2226/\circ\circ\circ$ quotient group, and $29R$ as a member of $*246/\circ\circ\circ$.

To embed this orbifold in the $*2226$ tiling of $\mathbb{H}^2$, we select parameters to form two euclidean parallelograms with a common edge. Set the $\mathbb{Z}\times\mathbb{Z}$ grid to be as located for the embedding of 2226, which we show again in Fig. 2.52: the point Q_A is located at the coordinate $\{0,1\}$, Q_B is at $\{1,1\}$ and Q_C is at $\{1,0\}$.

The vertex Q'_C (the 2–fold rotation that will not be a generator of 22223) must be chosen as an image of Q_C (not an image of Q_A or Q_B). This will ensure that the 22223 group constructed will have the correct generators to be a member of $*2226/\circ\circ\circ$. If Q'_C is chosen to be at an image of Q_A or Q_B, this will construct a 22223 group that is not a

Chamber Class	s0	s1	s2	m01	m12
A	E	**B**	E	8	4
B	**C**	A	**F**	8	4
C	**B**	D	**G**	8	6
D	**H**	**C**	**H**	8	6
E	A	**F**	A	8	4
F	**G**	E	**B**	8	4
G	**F**	**H**	**C**	8	6
H	D	**G**	D	8	6

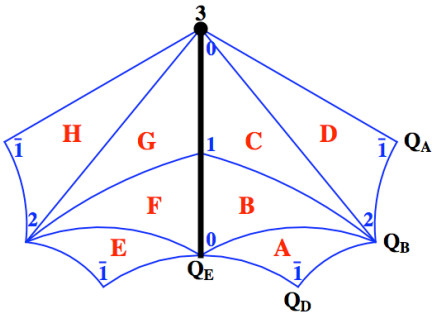

Figure 2.51: The encoding for the 22223 orbifold decoration having one edge pass from the 3–fold rotation to the 2–fold rotation marked Q_E. This tiling is called 22R as a member of the $*2226/\circ\circ\circ$ quotient group, or 29R as a member of $*246/\circ\circ\circ$.

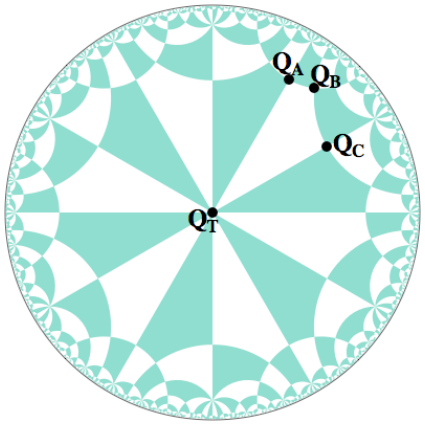

Figure 2.52: The reference frame generators for the 2226 symmetry group in the $*2226$ tiling. To establish an integer grid, Q_A, Q_B and Q_C are located at $\{0,1\}$, $\{1,1\}$ and $\{1,0\}$ respectively.

member of the $*2226/\circ\circ\circ$ quotient group. To ensure the correct group is obtained, we restrict the position of Q'_C to be a coprime integer pair $\{p,q\}$, where p is even (or 0) and q is odd (This restriction ensures that the deleted 2–fold rotation is an image of Q_C).

Fig. 2.53 shows the construction of a fundamental domain of the 22223 symmetry group by the parameters $Q'_C = \{0,1\}$ and $Q'_A = \{-1,0\}$, where the determinant of the parallelogram $ps_1 - qr_1 = (0) - (-1) = 1$ and $Q'_E = \{1,0\}$, where the determinant of the second parallelogram is $ps_2 - qr_2 = (0) - (1) = -1$. The geometry resulting from the embedding has additional symmetry of $*22223$, and the decoration is equivalent to one constructed on the $*22223$ orbifold, and shown in Fig. 2.50(b).

Consider the decoration of the orbifold shown in Fig. 2.51. The tiling boundary is composed of a single edge which passes from the 3–fold rotation to Q'_E. Thus the free tiling depends only on the position of Q'_E, and remains unchanged for distinct choices of Q'_A, Q'_B and Q'_D. We recall that the point Q'_E may be any coprime pair in the integer grid,

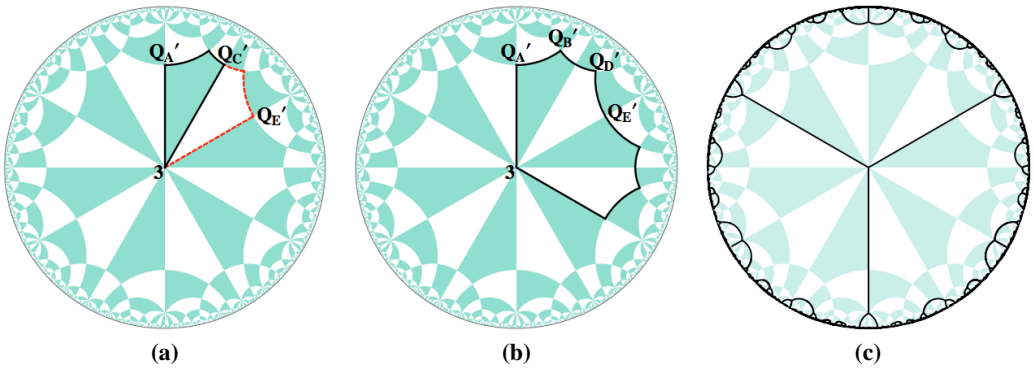

Figure 2.53: (a) Q'_C is the point $\{0,1\}$ in the $\mathbb{Z}\times\mathbb{Z}$ grid. Two quadrilaterals are constructed either side of this line, with $Q'_A=\{-1,0\}$ and $Q'_E=\{1,0\}$. (b) The resulting 22223 fundamental domain. (c) The free tiling resulting from the decorated and embedded orbifold, with increased symmetry of $*22223$.

$\{r_2,s_2\}$, where r_2 is odd, hence we need only select the position of Q'_E with this restriction to completely define the tiling. Further, by conjugacies of the $*2226$ grid, we need only consider coprime pairs in the positive–positive quadrant of $\mathbb{Z}\times\mathbb{Z}$.

Fig. 2.54 shows three examples of the decorated and embedded 22223 orbifold in the $*2226$ tiling of $\mathbb{H}^2$. The three embeddings are defined by the choice of Q'_E to be the following coordinates in $\mathbb{Z}\times\mathbb{Z}$: $Q'_E=\{1,1\}$ (namely $*2226_{22R}(1)$, shown in Fig. 2.54(a)), $Q'_E=\{1,2\}$ (namely $*2226_{22R}(2)$, shown in Fig. 2.54(b)), and $Q'_E=\{3,2\}$ (namely $*2226_{22R}(4)$, Fig. 2.54(c)).

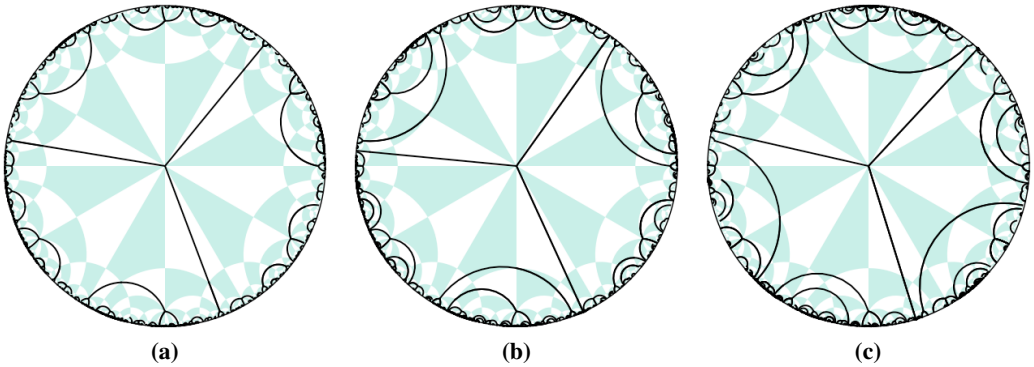

Figure 2.54: Three embeddings of the decorated 22223 orbifold in the $*2226$ tiling of $\mathbb{H}^2$to give three distinct free tilings. Q'_E is chosen to be (a) $\{1,1\}$: $*2226_{22R}(1)$, (b) $\{1,2\}$: $*2226_{22R}(2)$, (c) $\{3,2\}$: $*2226_{22R}(4)$.

The symmetry group 22223 is also a subgroup of the $*246$ symmetry group. Hence we can consider embedding the same decorated orbifold to be commensurate with the $*246$

tiling. This embedding follows the same process as for the $*2226$ embedding, however the location of the integer grid in $\mathbb{H}^2$ is slightly different (see examples in Fig. 2.47 for the location of the integer grid with respect to the $*246$ tiling). Fig. 2.55 shows a few examples, where the location of Q'_E is varied as follows:

1. $Q'_E = \{1,1\}$: $*246_{49R}(1)$ (Fig. 2.55(a))
2. $Q'_E = \{1,2\}$: $*246_{49R}(2)$ (Fig. 2.55(b))
3. $Q'_E = \{3,2\}$: $*246_{49R}(3)$ (Fig. 2.55(c))

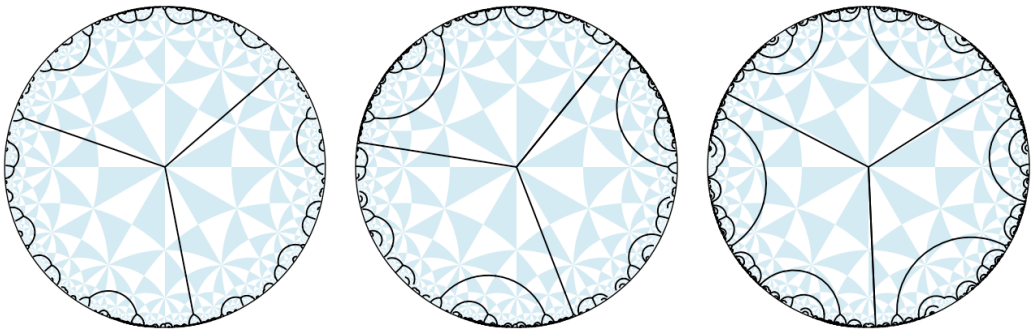

(a) **(b)** **(c)**

Figure 2.55: Three embeddings of the decorated 22223 orbifold in the $*246$ tiling of $\mathbb{H}^2$to give three distinct free tilings. Q'_E is chosen to be (a) $\{1,1\}$: $*246_{49R}(1)$, (b) $\{1,2\}$: $*246_{49R}(2)$, (c) $\{3,2\}$: $*246_{49R}(3)$.

This chapter presented a series of simply constructed free tilings. They were constructed to be commensurate with the symmetries of the genus–3 TPMS: the *P*, *D*, *G* and *H* surfaces. For a decoration of a Stellate orbifold, an infinite number of distinct embeddings into the surface charts exists, which all lead to distinct tilings of the surfaces. We presented the simplest embeddings of such tilings, along with the methodology to construct an infinite series of embedded tilings.

Free tilings are of interest because of the structures that result from their reticulation over the TPMS. In the case of regular ribbon tilings, the structures that result are the interpenetration of multiple net components. In the case of the complementary tilings, the vertex–free geodesic boundaries map to infinite 1–dimensional filaments, which are woven together in structures of varying complexity. This beautiful set of 3D structures will be presented in Ch. 3.